Interferometric Laser Imaging for Droplet Sizing Method for Long Range Measurements

A. García-Magariño[1], S. Sor[1], R. Bardera[1], J. Muñoz-Campillejo[1]

[1]National Institute of Aerospace Technology (INTA), 28850, Madrid, Spain

Abstract

A recent appendix in the aircraft regulations comprises testing supercooled large droplets impinging on its surfaces. For those tests, the size and distributions of droplets need to be characterized in icing wind tunnels. In this paper, the applicability of implementation of the "Interferometric Laser Imaging for Droplet Sizing" technique inside a wind tunnel with a 3 m x 2 m open elliptical test section has been discussed. Experiments have been conducted in the laboratory for the discussion at object distance of 1.6 m and 2.29 m and droplets diameters between 360 μm to 850 μm. All the streams were previously characterized by means of the shadowgraph imaging technique. A novel approach of the Interferometric Laser Imaging for Droplet Sizing technique where droplets are not fully defocused to avoid excessive overlapping is presented. Two new image processing approaches provide in general good results as compared to previous methods.

Key words: Interferometric Laser Imaging for Droplet Sizing, Droplet Sizing, Wind Tunnel Testing.

Corresponding author: A. Garcia-Magariño.

Email address: garciamga@inta.es , Phone: 00 34 91 520 20 31

1. Introduction

Even though aircraft icing has been considered as an important in-flight hazard since the early days of aviation [1], the limitations associated with the presence of supercooled large droplets (SLDs) in icing environments have not been included in the maximum flight envelopes until fairly recently [2], following the intensive studies that were conducted after the ATR-72 accident of 1994 regarding SLDs icing conditions. The latest review on aircraft icing also includes SLDs conditions [3]. A significant loss in aircraft performance, resulting even in loss of control, on account of the icing phenomena has been well documented [4-10]. Recent work still addressed the iced airfoils aerodynamic [11] and ice accretion models [12]. The ice accretion models are very sensitive to the liquid water content, the mean volume diameter and the droplet distribution [13]. Supercooled large droplets additionally add new threats due to the appearance of new phenomena substantially different associated with their large size such as droplet deformation and breakup prior to impact [14] being the formed ice more difficult to remove. Aircraft icing environments including SLDs have also been thoroughly characterized over the years based on direct clouds observation [10,15,16] in order to update the existing certification requirements. Specifically, the work presented by Cober and Isaac [16] provided enough data to undertake either numerical SLDs icing simulations or wind tunnel experiments, which could prove to be extremely helpful and provide invaluable information to better understand the ice formation. A hypothetical wind tunnel capable of effectively providing SLDs icing conditions without the scaling limitations reported by Anderson and Tsao [17] was designed by Orchard et al [18] by simulating both droplet velocities and temperatures through the wind tunnel for a given contraction ratio. However, the simulation of SLDs icing environments is not at all trivial with the current test facilities, especially when considering droplet diameters exceeding 500 µm [19] or a median volume diameter (MVD) higher than 190 µm [17]. The main problem lies in the correct generation and subsequent characterization of the SLDs cloud inside the wind tunnel. The cloud characterization consists of the determination of the droplets size, distribution, temperature and velocity. These droplets, that need to be characterized, are only

supercooled and no ice particles should be present. Therefore, problems associated to the formation of ice crystals, such as the ones described in Brunel et al [82], are not considered in this investigation.

While droplet velocities could be measured by means of particle image velocimetry (PIV) or particle tracking velocimetry (PTV) [83] and its temperatures assessed through simulation [18], the measurement and characterization of droplet size distributions through the test section is quite problematic. Direct imaging using backlit cannot be performed because in the transversal characterization either the camera or the backlit should be placed upstream thus modifying the flow. A Malvern Spraytec laser diffraction system has been used to provide in situ droplet size measurements in a wind tunnel [20], but it was placed inside the wind tunnel and other non-invasive techniques outside the wind tunnel are preferred [21]. In this context, there are a variety of optical techniques available such as the forward scattering spectrometer probe (FSSP) [22,23], the digital holography [84] or the phase doppler particle analyzer (PDPA) [24, 25] which allows simultaneous measurements of drop size and velocity. Also, recently a new extinction-based for drop sizing in optically dense diesel sprays for smaller droplet was proposed [26]. However, either the measurable diameter range, the sampling volume, or both, is too small. Nevertheless, there is also another non-invasive technique for droplets size measurement: the interferometric laser imaging for droplet sizing technique, hereafter referred as ILIDS technique.

The ILIDS technique, also known as interferometric particle imaging (IPI) or Mie scattering imaging (MSI) in the literature, is a non-invasive optical technique able to provide instantaneous measurements of sizes and spatial distributions of transparent spherical particles such as water droplets or bubbles within a certain field of view. Having its origins in the late 1980's [26–30], the ILIDS technique is based on the interferences between the scattered light from a coherently illuminated spherical and transparent particle. At certain scattering angles, depending on the polarization of the incident wave

relative to the observation plane, the reflected and refracted light are dominant over the rest of the scattered orders and two glare points appear in the focus plane [31]. Although in theory the droplet sizing is possible by simply measuring the distance between said points [32], the resolution requirements to do so with enough accuracy are high. However, if the glare points are observed in an out-of-focus plane, a fringe pattern arises due to the interferences between the reflected and refracted light. In the far-field, the number of fringes is directly proportional to the droplet diameter, and following the geometrical optics approach an expression can be derived [33,34]. Enough degree of defocus is needed in order to capture the whole fringe pattern and avoid measurement errors [33]. The validity of the geometrical analysis has been extensively studied [34,35], provided that the necessary conditions are met.

Although there are many advantages associated with the ILIDS method, one of the main disadvantages has always been the droplet concentration limitation due to the interferogram overlapping in dense sprays [36-38]. Since the work of Glover et al [30], who implemented for the first time the use of a laser sheet to capture multiple out-of-focus particle images, numerous studies followed in the subsequent years to further improve and refine the technique, especially regarding the overlapping problem. One of the most popular solutions in order to increase the maximum allowable droplet concentration is the so-called optical compression technique, which consists of the implementation of a cylindric lens in the optical system, thus simultaneously achieving the defocus of one dimension while keeping the focus of the other one [39,40]. Therefore, quasi-linear fringe patterns are captured, alleviating considerably the overlapping problem but at the expense of the loss of information. Furthermore, this method requires almost perfectly vertical fringes in order to accurately measure droplet sizes and is thus very sensitive to laser misalignments. Another possible solution, the global phase Doppler technique (GPD), was presented by Damaschke et al [41] by means of a second laser sheet intersecting the first one with a small inclination angle. Finally, another

important breakthrough in recent years has been the development of the so-called airborne laser interferometric drop sizer (ALIDS) to characterize cloud droplets during flight [42,43], combined with the capabilities of the ILIDS technique of measuring mixed flows (liquid and ice) along with irregular particles [44-46] and the development of real-time processing software [47,48].

Important advancements regarding the simulation of interferograms based on the Huygens-Fresnel principle have also taken place [49,50], which allows the direct comparison between simulated and experimental interferograms. In the most recent days, the efforts of the ILIDS technique development with regards to the overlapping problem, however, have been put to the image processing software [38,51,52], and is this approach the one which has inspired the present work. To do so, two algorithms are key to the developed image processing software: the Hough transform [53], which is a very robust algorithm capable of adequately detecting circles even with incomplete circle edges evidence [54]; and the Watershed transform [55], which is a powerful segmentation algorithm that can be used to effectively distinguish different objects even in very complex and problematic images [56-59].

In this context, the aim of this paper is the assessment of a future implementation of the technique inside a wind tunnel and the corresponding limitations in terms of object distance or camera resolution, with the ultimate goal of effectively characterizing the spatial size distribution of simulated SLDs inside a wind tunnel. The potential for simultaneously measuring both droplet size and velocity by means of both ILIDS and PIV techniques has already been presented with promising results [39,60-62]. In fact, the recent work of Kosch et al [63] was dedicated to correcting the center discrepancies between ILIDS and PIV techniques. Furthermore, according to the cloud observations reported [10,15,16], the formation of SLDs is associated with very low particle concentrations and, therefore, a typical ILIDS setup has been used in the present work.

First, an introduction to the theoretical background of the ILIDS technique will be made, followed by the design of the experiments. Then, the developed image processing software will be explained including several methods. Both the obtained experimental images and the processing results will then be presented and discussed. Finally, conclusions are given showing promising results.

2. Theoretical Background

The ILIDS technique is based on the regular oscillatory properties of the rays of light scattered by a spherical and transparent particle, such as a water droplet or a bubble, when illuminated by a coherent light source, and the subsequent interferences between them. Each incident light ray is scattered by the particle into a series of different beam paths propagating in multiple directions, both in the forward and backward-scatter regions, as can be seen in Fig. 1. The scattering order p is defined based on the number of interactions between each ray path and the particle.
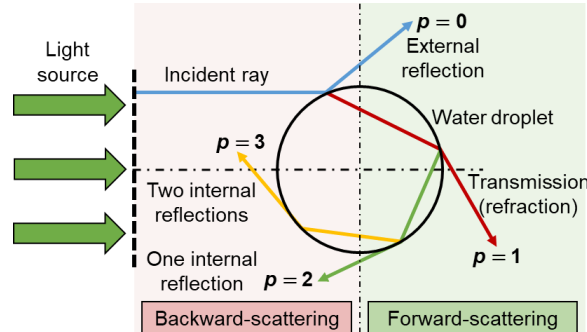
Fig. 1 Ray paths of the first 4 scattering orders in a coherently illuminated water droplet according to geometrical optics.

The regular oscillatory properties of the scattered light can be rigorously described by the Lorenz-Mie theory (LMT) [64,65]. For a given droplet size, the scattering intensity, and thus the contribution of each component, will depend on the scattering angle and the polarization of the laser source relative to the observation plane (Fig. 2). For a perpendicularly polarized incident wave and a scattering angle of around $\theta = 67°$, the intensities of the reflected and refracted light are equal and clearly dominant over the

other scattered rays. The same condition is satisfied under parallel polarization for a scattering angle of approximately $\theta = 82°$, although the corresponding scattered intensity is at least one or two orders lower. A fringe pattern or interferogram emerges from the interferences between the refracted and reflected light in the out of focus images at the aforementioned off-axis angles, from which the droplet size could be determined. The problem is then reduced to the interference between two single rays of light, as in Fig. 2.
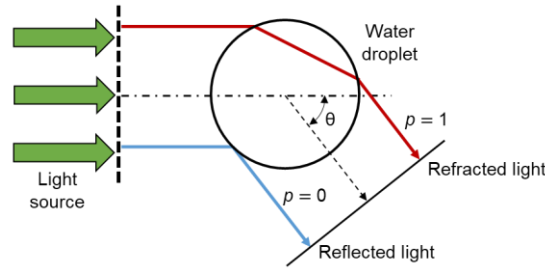

Fig. 2 Optical ray paths of the first 2 scattering orders (reflected and refracted light) for a given scattering angle according to geometrical optics.

The quality of the resulting interferogram and thus the fringe visibility depends on the intensity of said scattered rays, which is also a function of the droplet size, increasing with the diameter. Such a dependence can be seen in Fig. 3, in which the first two scattering orders for 3 different droplet sizes – 100 µm, 400 µm and 800 µm – are represented for both a perpendicular and parallel polarization of the laser sheet. This fact hinders the simultaneous study of large and small droplets, and the problem is further aggravated in the case of parallel polarization since the optimal off-axis angle is also affected by the drop diameter. An evaluation of fringe visibility as a function of the scattering angle and droplet size was conducted in Ref. [69]. Under perpendicular polarization, there is a reasonably wide range of scattering angles (near 67°) in which fringe visibility remains high and the dependence of drop size is low, and no third glare point effect appears [70].
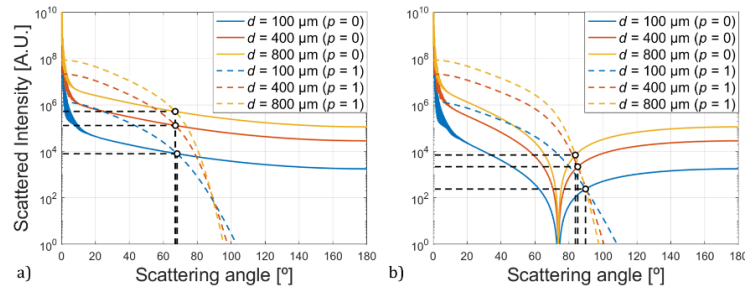
Fig. 3 Evolution of the intensity of the first 2 scattering orders with the scattering angle for 3 different droplet sizes with a) perpendicular polarization and b) parallel polarization of the incident laser sheet.

For both the reflected and refracted light, a propagation cone is formed towards the camera lens with a collecting or aperture angle α. After the light passes through the camera lens, both propagation cones converge towards the image plane. As the defocus length l_d increases, the interference between them arises in the overlapping region, thus producing the fringe pattern. In Fig. 4 the typical ILIDS arrangement is shown, along with the propagation cones from the reflected and refracted light, the most relevant parameters of the optical system and the fringe pattern formed in the overlapping region.
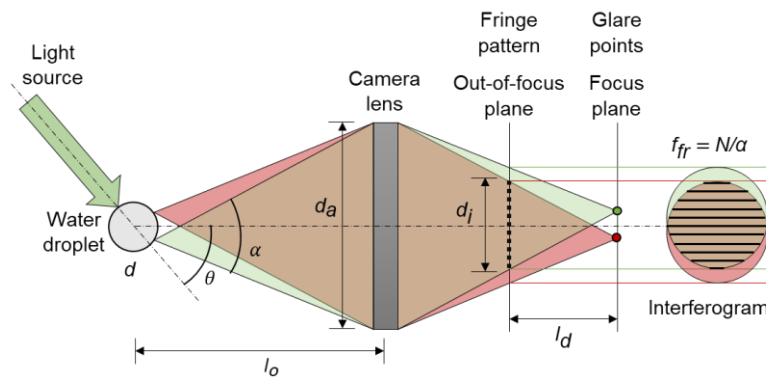

Fig. 4 Typical ILIDS optical imaging arrangement producing two glare points in a focus plane and its corresponding fringe pattern in an out-of-focus plane.

In the defocused plane, the reflected and refracted rays' propagation cones will be captured as two circles overlapping each other with fringes emerging in between them. The image size d_i will not depend on the actual droplet size but on the optical imaging arrangement. For a given optical arrangement, as the defocus length l_d or the effective aperture of the camera lens d_a increases, so does the image size d_i, as can be visually

seen in Fig. 4. Fig. 5 also shows the effects of varying the defocus on the degree of overlap between the propagation cones. At a certain defocus distance, the propagation cones will be virtually merged, which while allowing an easiest data analysis of the out-of-focus images come at the expense of an increased image size. Furthermore, the larger the droplet, the higher the required defocus, since the two glare points will be farther away from each other. Therefore, when capturing droplets of very diverse sizes, a full overlap of the propagation cones will not be simultaneously achieved for all of them [41]. An approach based on the partial defocus of the droplets would reduce image size and potentially allow for simultaneous measurements of different droplet sizes.
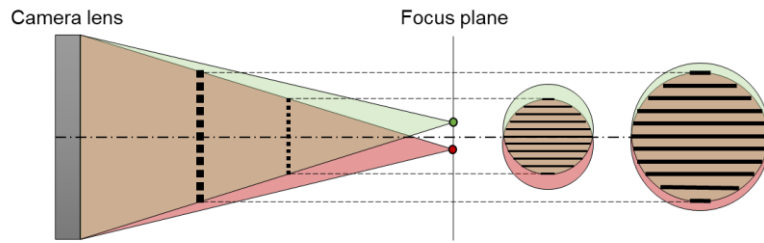
Fig. 5 Evolution of the particle image size and circles overlapping with the defocus distance.

The droplet diameter is directly related to the angular inter-fringe spacing, that is, to the number of fringes of the interferogram. That relationship can be determined via a geometrical optics analysis by obtaining the phase difference between the reflected and refracted ray paths and is given by the following expression, put forth by Hesselbacher et al [28] and Roth et al [29]:

$$d = \frac{2\lambda N}{\alpha}\left[\cos\left(\frac{\theta}{2}\right) + \frac{n\sin\left(\frac{\theta}{2}\right)}{\sqrt{n^2+1-2n\cos\left(\frac{\theta}{2}\right)}}\right]^{-1} \tag{1}$$

where d is the particle diameter, N is the number of fringes, λ is the wavelength of the laser sheet, α is the collecting angle of the optical arrangement, θ is the scattering or off-axis angle and n is the relative refractive index corresponding to a water droplet in air. The fringe frequency-count to particle size relationship could also have been obtained with exact light scattering theories with a higher accuracy [86], however the geometrical

theory provides the enough accuracy required in this case. The fringe frequency is defined as $f_{fr} = N/\alpha$. Note that in the previous expression the droplet diameter does not depend on the scattered light intensity. The previous equation is valid whenever the size parameter satisfies the condition $\pi d_p/\lambda > 10$-20, which would be the minimum measurable droplet size, and the particle and medium refractive index differ enough from each other, as stated by H. C. van de Hulst [71]. The maximum measurable droplet size will be constrained by the Nyquist criterion, which establishes that each fringe within the interferogram needs to be covered by at least two pixels, and therefore $n_{pix} \geq 2N$, where n_{pix} is the width of each fringe pattern, measured in pixels. The larger the droplet, the higher the necessary image width.

In an optical arrangement such as the one presented in Fig.4, the collecting angle α can be determined by the expression $\alpha = 2\,a\sin(d_a/2l_o)$. However, no isolated lens, but rather an assembly of lenses within the camera objective, has been used. Therefore, a simplified expression of the effective aperture angle α as a function of the numerical aperture NA and the linear magnification ratio M was derived based on the work of Mounaïm-Rousselle et al [72]. Given that the effective lens aperture can be taken as $d_a = f/NA$, where f is the camera focal length and NA the chosen numerical aperture, and by assuming a single thin lens simplification with which the focal length f, the object distance l_o and the imaging distance l_i can be related by $\frac{1}{f} = \frac{1}{l_o} + \frac{1}{l_i}$, the following expression is derived:

$$\alpha = 2\,a\sin\left(\frac{M}{M+1} \cdot \frac{1}{2NA}\right) \tag{2}$$

in which the linear magnification has been taken as the ratio between image and object distance, $M = l_i/l_o$.

3. Requirements regarding Object Distance.

Both the experiments and the analysis were carried out with a view to undertake them inside the wind tunnel number 1 of INTA, which is a closed return low-speed wind tunnel capable of reaching an airspeed up to 60 m/s with a freestream turbulence intensity lower than 0.5 % and a 3×2 m^2 open elliptical test section, with the major axis of the ellipse matching the width of the tunnel. Depending on the off-axis angle and the orientation of the laser sheet relative to the airflow, the minimum object distance requirement might vary, as represented in Fig. 6, ranging from a minimum of 1.5 m to a maximum of almost 4 m. Since the horizontal axis of the wind tunnel is 3 m long, this requirement would imply a minimum distance of 1.5 m between the camera and a droplet located at the center of the tunnel, provided the laser sheet were to be parallel to the flow and the off-axis angle equal to 90º. For a scattering angle of $\theta = 67°$ the minimum required object distance would be approximately $l_o = 1.6$ m. However, the transversal spatial droplet size distribution is also needed, in which only the latter could be of use since the former would interfere with both the flow and any scale model inside the test section. Therefore, the minimum object distance would significantly increase up to about 3.8 m.
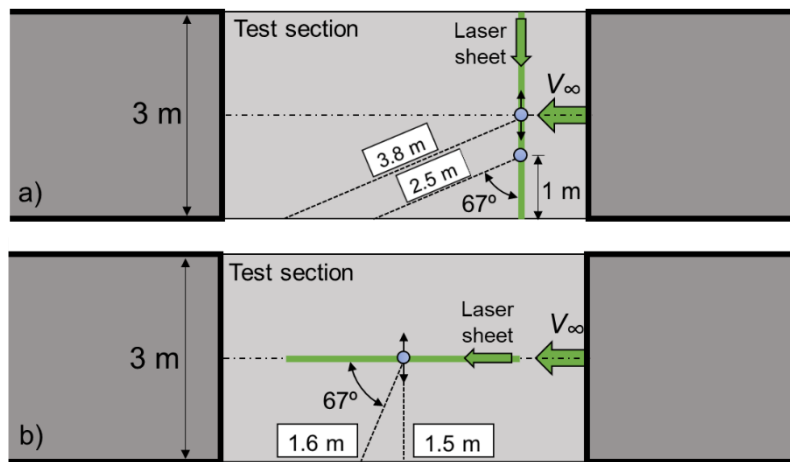
Fig. 6 Representation of possible ILIDS configuration inside a wind tunnel and its necessary minimum object distances with the laser sheet a) perpendicular and b) parallel to the wind tunnel airflow.

Such a requirement is an enormous limitation to the ILIDS technique. As the object distance increases, the resulting field of view, and thus the camera resolution requirement, substantially raises as well, hence considerably restricting the maximum

measurable droplet size. Nevertheless, several alternative configurations could be used in order to reduce the object distance, particularly when considering a transversal laser sheet. Instead of aligning the field of view with the wind tunnel axis, it could be slightly moved towards the test section border. If a reasonable margin of 1 m between the field of view center and the test section border is considered, the minimum object distance would now be of only 2.6 m (see Fig. 6). The same distance could be obtained by implementing a vertical optical arrangement, since the wind tunnel height is only 2 m long. In any case, the necessary object distance is still very high, and therefore an assessment of this limitation needs to be made in order to evaluate the viability of undertaking wind tunnel experiments.

4. Description of the experiments

The experiments have been conducted at Instituto Nacional de Técnica Aeroespacial (INTA) by means of the ILIDS technique. The experimental setup follows a typical ILIDS arrangement as shown schematically in Fig. 7. Three different monodispersed streams of droplets were generated by using a Rayleigh-based monodisperse droplet generator, which exploits the inherent instability of a round liquid jet when excited at a certain wavelength [73]. The water jet of the droplet generator is supplied by a pressurized water tank which is connected to an air compressor. The experiments have been carried out in a laboratory under controlled conditions of calm atmosphere. A vertical laser sheet with a typical thickness of 0.5 mm and a wavelength of 532 nm generated by a neodymium-doped yttrium aluminium garnet (Nd:YAG) laser beam passing through a combination of three semi-cylindrical lenses and a spherical one, with focal lengths of -200 mm, -100 mm, -50 mm and 1000 mm, respectively, illuminated the stream of droplets. The laser used was a Surelite Model SL-10, with a frequency of 10Hz and a power of 150 mJ per pulse. The scattered light from the droplets was collected by a NIKKON D800E, which is a high-resolution camera with a total of 36.3 effective megapixels and a 35.9×24.0 mm CMOS image sensor, equipped with an AF-S NIKKOR 300mm f/2.8G ED VR II camera

lens. The area of 1 pixel in the CMOS sensor, called S_p, has a value of 23.72 μm^2. An effective lens aperture of f/4 was chosen in order to collect enough scattered light from the droplets. The laser sheet was perpendicularly polarized to achieve maximum fringe visibility as discussed in the theoretical background. The experimental setup is presented in Fig. 7, in which every relevant component is shown.
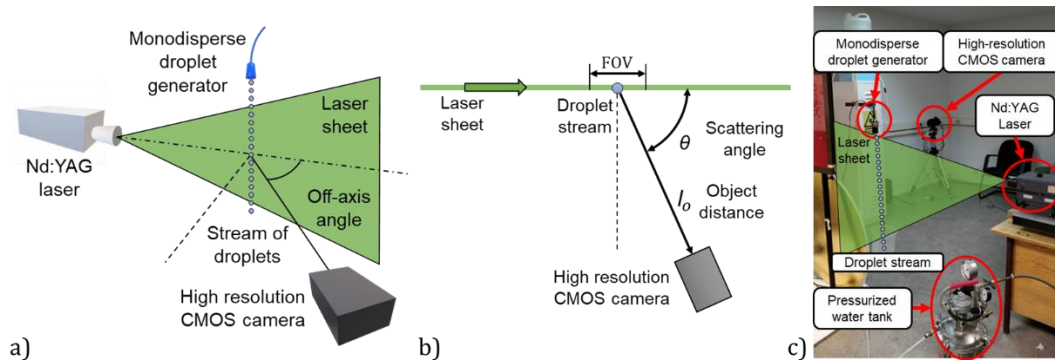

Fig. 7 Scheme of the ILIDS experimental setup as seen a) from the side; b) from above and c) actual ILIDS experimental setup

Two different configurations have been tested. The chosen object distances were 1.6 m and 2.29 m for configuration 1 and 2, respectively, whereas the off-axis angle was 71º and 67º, respectively. The pixel resolution was 16.1 μm/pix and 32.2 μm/pix in each configuration, and thus the resulting field of view was $FOV_1 = 11.9{\times}7.9$ cm^2 and $FOV_2 = 23.7{\times}15.8$ cm^2. Given that both the field of view and the CMOS sensor size are known, the linear magnification ratio M of each optical configuration can be calculated, being $M_1 = 0.302$ and $M_2 = 0.152$, respectively. The magnification ratio in configuration 2 is half the magnification in configuration 1, which implies that an increase in object distance of about 45% results in effectively doubling both dimensions of the corresponding field of view. Consequently, in order to achieve the same image quality, the camera resolution would need to be 4 times higher.

A total of three different droplet sizes have been studied. The sizes of the droplets have been chosen to cover the typical size of droplets encountered in the SLD clouds that need to be simulated in the wind tunnel. The stream of largest droplets was studied in

configuration 1, whereas the other two smaller droplet sizes were studied in configuration 2. The size of the three studied streams of droplets was characterized in advance by means of the shadowgraph imaging technique. For that purpose, each stream of droplets was illuminated from the back with a LED light source (backlighting technique) and captured with the abovementioned camera setup. The data processing of the shadowgraph images was comprised of three main stages: 1) image binarization using a locally adaptive threshold based on the local mean intensity in each pixel and its neighborhood [74] to locate all the droplets; 2) isolation of each detected separate droplet and 3) measurement of each droplet size using Otsu's method [75] to binarize the isolated droplet image. The holes corresponding to the bright point in the middle of the droplets were filled. The detailed process of measuring each droplet size can be observed in Fig. 8 for a stream of droplets. An example of the isolated droplet images for the three droplets sizes and the equivalent diameter measured for each droplet is shown in Fig. 9.
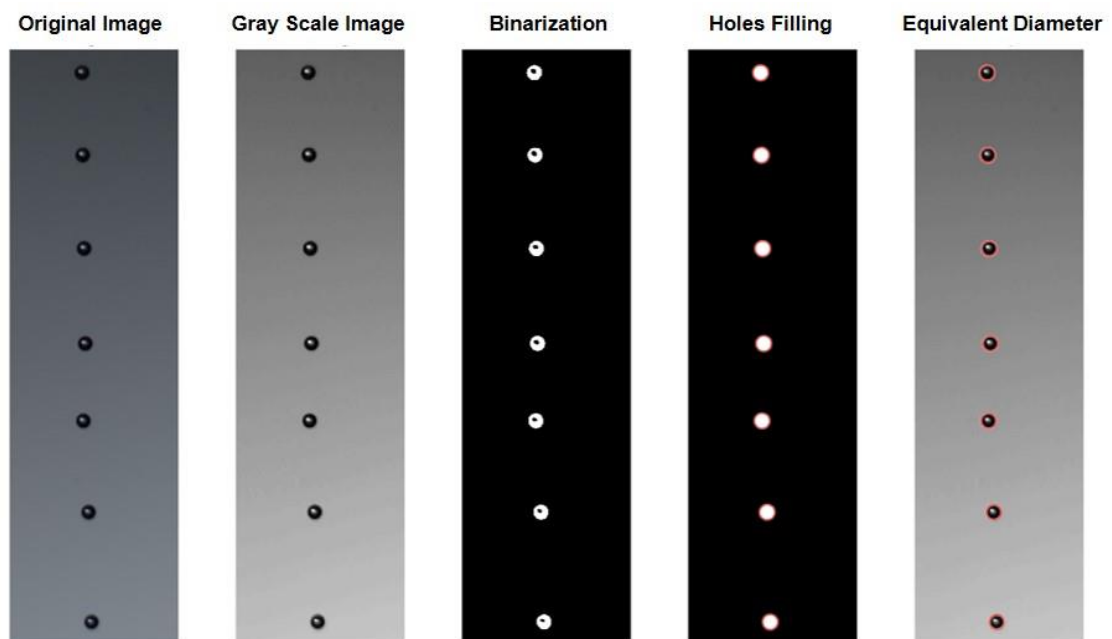
Fig. 8 Image processing of a monodispersed stream of droplets captured with the shadowgraph imaging technique
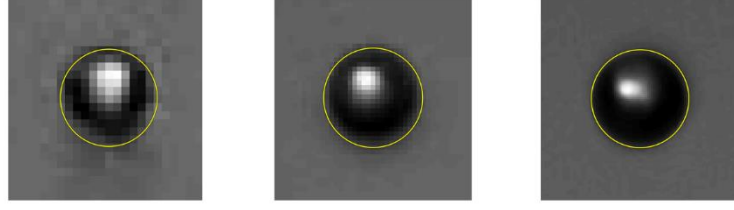
Fig. 9 Extracted fragments from the shadowgraph images of the droplet streams with the detected equivalent diameters underlined for three droplet sizes (smaller to larger from the left to the right).

The droplet diameter is calculated counting the number of pixels occupied by the area of the droplet image after binarization, N_p, knowing the magnification, M, and assuming that the droplet is spherical, as follows:

$$d = \frac{1}{M}\sqrt{\frac{4}{\pi}N_p S_p} = F(M, N_p, S_p)$$

The droplet size uncertainty, U_d, can be calculated as follows:

$$U_d^2 = \left(\frac{\partial F}{\partial M}u_M\right)^2 + \left(\frac{\partial F}{\partial N_p}u_{N_p}\right)^2 + \left(\frac{\partial F}{\partial S_p}u_{S_p}\right)^2$$

Where u_M, u_{N_p} and u_{S_p} are the uncertainties in the measurement of: the magnification, the number of pixels and the pixel area respectively. The most important contribution was due to the measurement of the number of pixels occupied by the droplet image, which consisted of the systematic error term and the random error term, being the systematic error negligible compared to the random error:

$$\left(\frac{\partial F}{\partial N_p}u_{N_p}\right)^2 = \left(\frac{2}{\pi}\frac{S_p}{M^2 \overline{d}}\right)^2\left[\left(u_{N_p}\big|_{syst}\right)^2 + \left(u_{N_p}\big|_{random}\right)^2\right]$$

Where overbar indicates averaged quantities, $u_{N_p}\big|_{syst}$ was 0.5 pix and $u_{N_p}\big|_{random}$ has been calculated as follows:

$$u_{N_p}\big|_{random} = t_{n-1,0.95}\frac{\sigma_{N_p}}{\sqrt{n}}$$

Being $t_{n-1,0.95}$ the t-student function, σ_{N_p} the standard deviation of the measurements and n the number of measurements, which ranged between 15 and 60 measurements. Due to the considered field of view being so large, a homogeneous illumination within

the whole captured background was not possible, since the LED source was circular and its light intensity varied with the radius, as shown in the Fig. 10a. The influence of the background illumination in the characterization can be assessed by representing the measured diameter as a function of the vertical position of the droplets within each shadowgraph image, as presented in Fig. 10. The maximum experimental variance was on the order of 15% of droplet diameter. The uncertainties are 6 μm for the small droplets, 10 μm for the medium-sized droplets and 8 μm for the large droplets, which are considered acceptable for the purpose of this investigation. The reason for the larger uncertainty for medium droplets relies on a larger dispersion of the droplets' diameter in the generation of the stream of droplets, which increases the random error in the measurement.
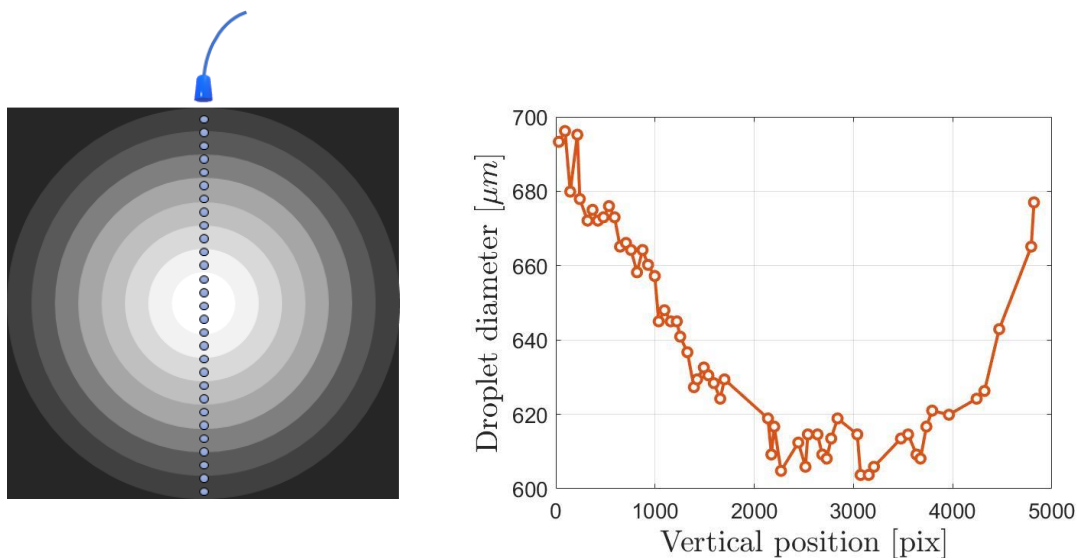
Fig. 10 A sketch of the illumination source on the left. Evolution of the measured droplet diameter with the vertical position of each droplet within the shadowgraph image on the right.

Finally, the test matrix of the experiments can be observed in Table 1. An overview of the main parameters involved in the experiments and the measured droplet size of each stream of droplets via shadowgraph imaging technique are summarized in Table 1. Collecting angles in each configuration were obtained as stated in Eq. (2) with the aperture number being $NA = 4$ and the magnification ratios being $M_1 = 0.302$ and $M_2 = 0.152$, respectively.
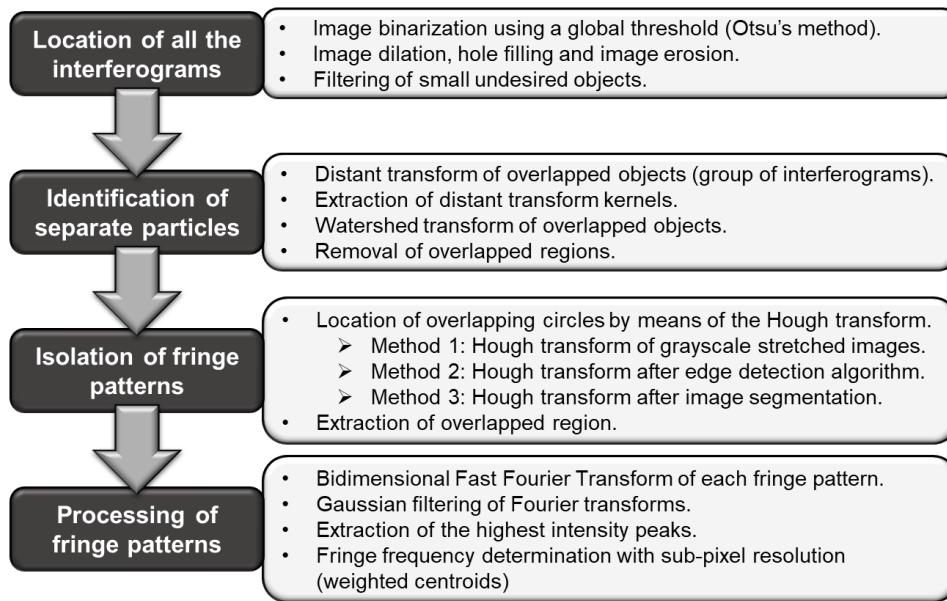
Table 1 Test matrix

| Droplet Diameter	Field of View	Pixel Resolution	Off-axis Angle	Collecting Angle	Object Distance
363 $\pm$ 6 µm	23.7×15.8 cm^2	32.2 µm/pix	67°	1.89°	2.29 m
658 $\pm$ 10 µm	23.7×15.8 cm^2	32.2 µm/pix	67°	1.89°	2.29 m
841 $\pm$ 8 µm	11.9×7.9 cm^2	16.1 µm/pix	71°	3.22°	1.6 m

5. Image Processing Proposed Method

A novel approach regarding the ILIDS technique is proposed in the present work based on the droplets not being fully defocused, from which a main particularity is derived: the presence of two circular disks corresponding to the scattered light propagation cones, as stated in Section 2. While somewhat hampering the image processing, this approach reduces the size of the interferograms and thus alleviates the overlapping problem. In order to address this particularity, a dedicated image processing software has been developed in MATLAB and is presented as an alternative way of analyzing ILIDS images. For real sprays, the atomization is a random process so a number of images needs to be recorded and processed. However, this investigation is limited for mono-dispersed drops and therefore, only a limited number of images have been analyzed. The flowchart of the whole proposed image processing software is shown in Fig. 11.

| Location of all the interferograms | • Image binarization using a global threshold (Otsu's method).
• Image dilation, hole filling and image erosion.
• Filtering of small undesired objects. |

| Identification of separate particles | • Distant transform of overlapped objects (group of interferograms).
• Extraction of distant transform kernels.
• Watershed transform of overlapped objects.
• Removal of overlapped regions. |

| Isolation of fringe patterns | • Location of overlapping circles by means of the Hough transform.
  ➢ Method 1: Hough transform of grayscale stretched images.
  ➢ Method 2: Hough transform after edge detection algorithm.
  ➢ Method 3: Hough transform after image segmentation.
• Extraction of overlapped region. |

| Processing of fringe patterns | • Bidimensional Fast Fourier Transform of each fringe pattern.
• Gaussian filtering of Fourier transforms.
• Extraction of the highest intensity peaks.
• Fringe frequency determination with sub-pixel resolution (weighted centroids) |

Fig. 11 Flowchart of the presented image processing software.

## 5.1 Location and identification of separate interferograms

The first step of the image processing software is the location and identification of each separate particle, with the first stage being the binarization of the interferograms. A representative fragment extracted from an experimental image comprising five different interferograms with several degrees of overlapping (an isolated interferogram, two mildly and two more severely overlapped interferograms) is shown in Fig. 12a to better illustrate the process, although only the grayscale image (see Fig. 12b) will be used in the analysis. Since the background is homogeneous, global binarization may be used. A threshold well below the one obtained by Otsu's method [75] is selected to ensure that the whole interferogram is contained (see Fig. 12c). To further improve the results, a postprocessing of the binarized image consisting of morphological such as image dilation, erosion or hole filling [76] is also carried out, as shown in Fig. 12d, and small spurious objects that may appear are filtered. The object used for the image dilation was a cross of size 3 pix, and the object used for the image erosion was a disk of size 1 pix.
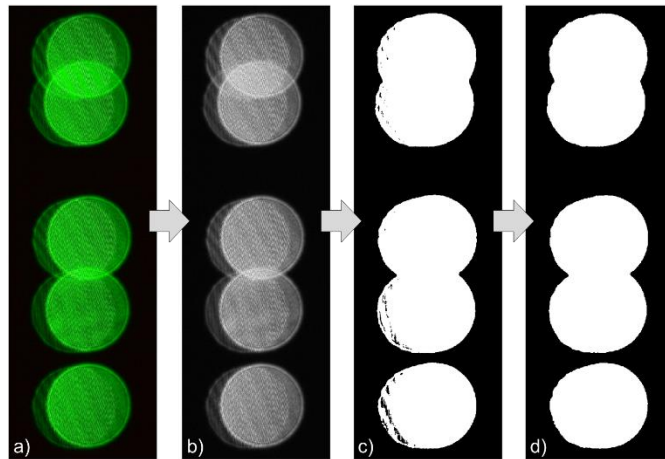
Fig. 12 First stage of the image processing: a) Extracted fragment from ILIDS images; b) converted grayscale image; c) globally binarized image and d) binarized image after postprocessing

Since overlapping interferograms will appear as one large merged object, the second stage is the separation of these interferograms. Fig. 13 shows the main steps involved in this second stage. During step 1, the distance transform of the previously binarized picture is obtained (see Fig. 13b). Then, in step 2, the extended-minima transform [77] of the complement of the distance transform is computed and its kernels are extracted (see Fig. 13c). The extracted kernels are connected groups of pixels whose intensity is constant within a specified range, with all the external pixels having higher values. The smaller the range, the smaller the extracted kernels. Shallow minima from the distance transform is thus removed. In step 3, the watershed transform [55] is then computed with the extracted kernels from the distance transform as input, thus effectively separating the merged objects when combined with the original binarized image (see Fig. 13d). The watershed transform searches for the ridgelines of an image by considering the bright and dark pixels as high-elevation and low-elevation regions, respectively. The use of the extracted kernels instead of the distance transform itself prevents the watershed transform from oversegmenting the image. In step 4, the centroid of each separate object is determined (see Fig. 13e). It should be noted, however, that the objective is not yet to accurately locate the center of each interferogram. A mere approximation will suffice at this point. In step 5, based on the centroid and the information from each object before

and after the Watershed transform, an equivalent diameter is derived and represented in order to remove overlapping regions (see Fig. 13f). Finally, in step 6, the overlapping regions of each interferogram are removed (see Fig. 13g).
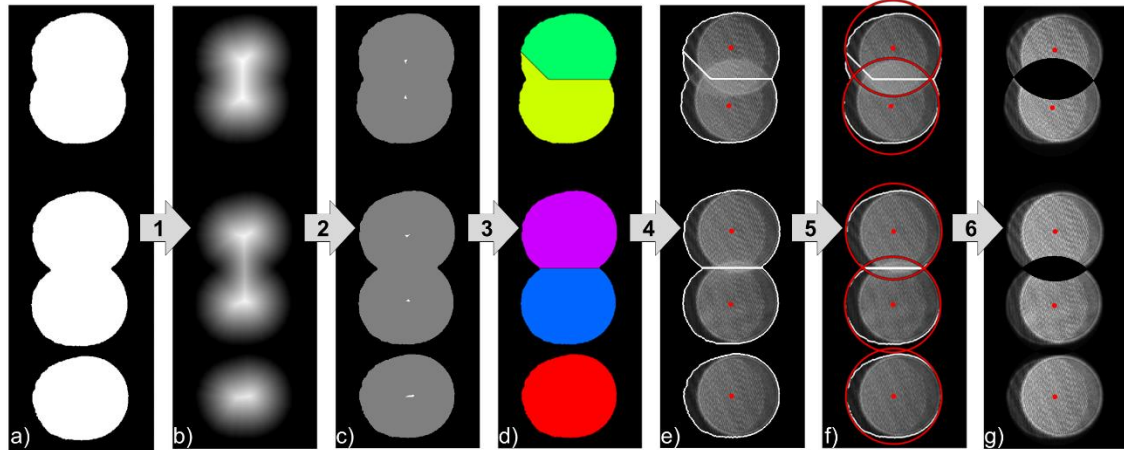
Fig. 13 Second stage of the image processing: a) Binarized image; b) distance transform; c) distance transform kernels; d) Watershed transform; e) grayscale image with centroids and particles boundaries underlined; f) the equivalent diameter chosen and g) particle images after removal of overlapped regions.

The presented method proves to be very robust and is able to identify distinct particles even with severely overlapped interferograms, as showed in Fig. 14.
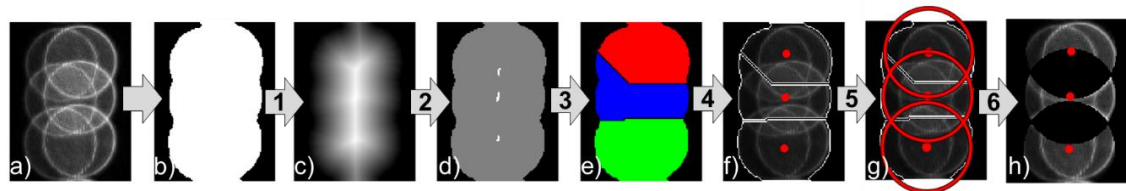
Fig. 14 Implementation of the first and second stages to severely overlapped interferograms.

5.2 Isolation of fringe patterns

Having located and identified every drop image, the next step is the isolation and subsequent extraction of each fringe pattern in order to determine fringe frequency and undertake droplet sizing. Three methods based on the Hough transform [53] are proposed in order to locate the two circles producing the fringe pattern

5.2.1 Method 1

This first method is based on the direct application of the Hough transform. Each interferogram is first subjected to a linear contrast stretch together with a Gaussian blur and an unsharp filter (see Fig. 15b). The Gaussian blur is meant to erase as much fringe evidence as possible, while the unsharp filter and the contrast stretch is intended to significantly increase edge evidence of the circles. The chosen parameters in each image filter will have a great influence on the results, but unfortunately, there is not a unique combination that provides good generalized results for all the cases at the same time. A careful design of the filters is therefore needed, since while a certain unsharp filter might adequately sharpen the circle edges, it could also favor the creation of undesirable noise within the fringe pattern. On the other hand, while a high standard deviation Gaussian filter will effectively erase most of the fringe evidence, it could also compromise the edge visibility.

After the preprocessing, the Hough transform is applied. The effectiveness of this method is very dependent on several parameters of the Hough transform algorithms such as the sensitivity, the edge threshold or the radii range in which the transform searches for circles. Among them, the radii range is the main point of concern: small changes in the radii range may result in relatively large changes in the located circles radii. In order to avoid such an inconvenience, the algorithms have been developed in a staged manner, with the radii range narrowing after each stage. First, a relatively wide initial range is considered according to the interferograms' width and height. The candidate circles of the Hough transform are sorted in the MATLAB in-built algorithm according to an accumulator array. The higher this magnitude, the higher the probability of being an adequate circle. Therefore, the strongest circle radio will act as new reference as the range narrows around it, the Hough transform is used again, and so on. When the strongest circle radio matches the reference's, the loop stops, and the two strongest circles are selected. A series of acceptance criteria have also been implemented in order to filter spurious circles that may have been erroneously detected by the algorithm. For

example, taking the strongest circle as reference, all the detected circles that are quasi-concentric or whose center is almost directly above or below the reference are filtered. A minimum and a maximum horizontal and vertical separation between the two strongest circles is also selected. These criteria have proven to be quite important when filtering spurious results, particularly considering that the image processing software has been developed to be automated. The results of this approach are shown in Fig. 15c.
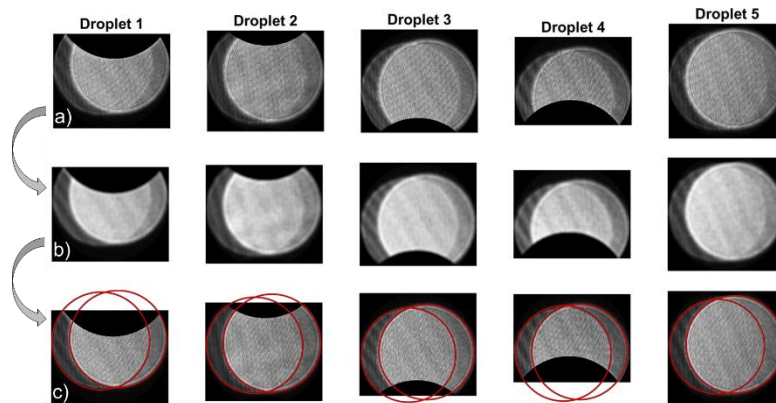
Fig. 15 Location of circles in interferograms using the first proposed approach: a) isolated interferograms; b) linear contrast stretch of the images and c) circle detection using Hough transform.

5.2.2 Method 2

The second method is almost directly based on the work of Glover et al [30], which was the first application of the ILIDS technique in a bidimensional manner. As in Method 1 above, a linear contrast stretch, a Gaussian filter and an unsharp filter are implemented (see Fig. 16b), although an additional step is added: an edge detection by means of the Canny algorithm [78] (see Fig. 16c). The strongest edges are easily detected; however, the algorithm struggles to find fainter edges. Fig. 16c also shows the differences in the algorithm's behavior for a given set of parameters – namely the sensitivity and the edge threshold – between different interferograms. While only the circle edges are present in the leftmost picture (droplet 1), a considerable amount of noise appears in the rightmost picture (droplet 5). On the other hand, several concentric edges arise in some cases due to the width and intensity of the interferogram rings, thus creating a potential source of

error and uncertainty. Finally, the Hough transform is applied. Depending on which concentric circle is detected, the extracted fringe pattern width will vary (see Fig. 16d).
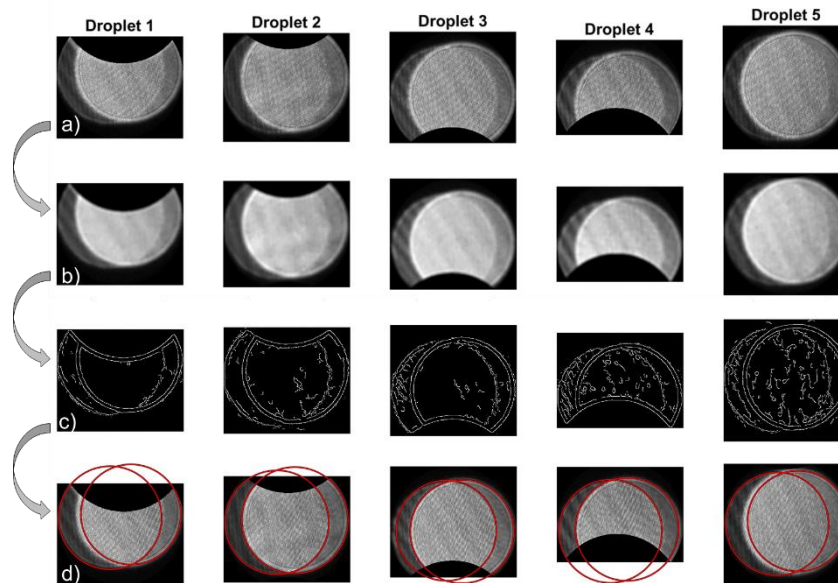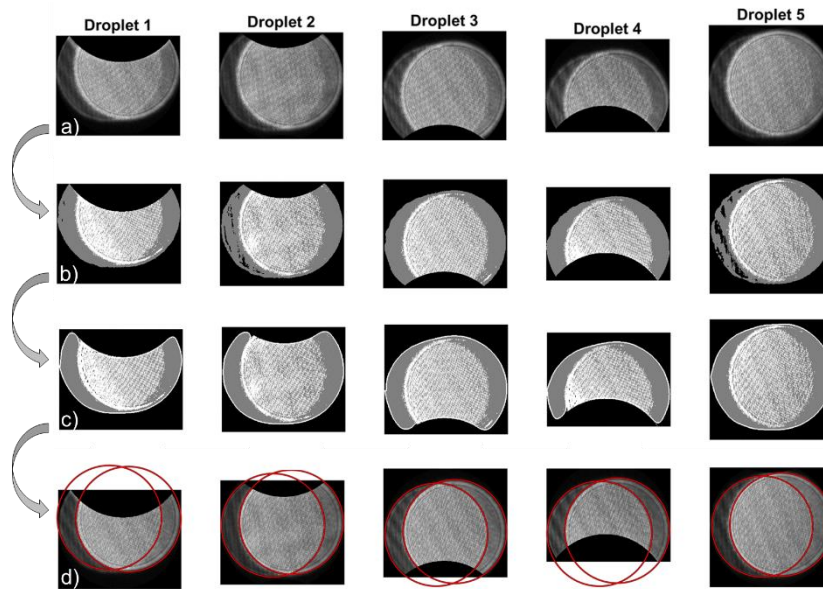

Fig. 16 Location of circles in interferograms using the second proposed approach: a) isolated interferograms; b) Gauss and unsharp filter of the images; c) edge detection using Canny algorithm and d) circle detection using Hough transform

5.2.3 Method 3

The third method is a novel approach meant to extract edge information from both the outer and the inner boundaries of the interferogram, thus easing the location of the circles by the Hough transform. This method is based on a prior image segmentation of the interferograms by means of a multilevel Otsu's threshold, as shown in Fig. 17b. As in the global binarization conducted in the first stage of the image analysis, the lower Otsu's threshold needs to be adjusted so as to correctly segment the whole interferogram. Since the effectiveness of the Hough transform algorithms significantly increases when the desired circles are either much brighter or much darker than the background, the second level of the image segmentation – gray area in Fig. 17b – is subjected to a postprocessing consisting of morphological operations and a first order Savitzky-Golay filter [79], and its external boundary is then extracted and added to the first level of the segmented image – white area in Fig. 17b – as presented in Fig. 17c. Although it could improve the results

23

in certain cases, no postprocessing of the first level is conducted in order to avoid significant differences in the algorithm's behavior when implemented in interferograms with different characteristics. The Hough transform is then used to detect the corresponding circles in the segmented image. The results are shown in Fig. 17d.

Fig. 17 Location of circles in interferograms using the third proposed approach: a) isolated interferograms; b) segmented interferograms with three levels; c) segmented interferograms after postprocessing and d) circle detection using Hough transform

5.3 Extraction and processing of the fringe pattern

Once the two circles from each interferogram have been adequately isolated, the removal of the non-overlapping regions is conducted to isolate the fringe pattern. One of the most important advantages of the ILIDS method is the ability of the Fast Fourier Transform (FFT) to extrapolate fringe frequency even with incomplete fringe patterns, provided its width and height are known. Therefore, a zero padding of the extracted images has been carried out in Fig. 18c, in which what should be the entire pattern as detected by the Hough transform has been underlined. This allows the measurement of both vertically and horizontally overlapped interferograms. The definition of the degree of overlapping of each isolated fringe pattern region is the ratio between the overlapped and total fringe pattern area as follows:

24

$$\gamma_{fp} = \frac{\text{Overlapped fringe pattern area}}{\text{Total fringe pattern area}} = \frac{\sum A_{overlap}}{A_{total}} \qquad (3)$$

A visual explanation of this parameter is shown in Fig. 18d. In the case of multiple overlapping, this means that the sum of all the overlapped regions divided by the total fringe pattern area will give the degree of overlapping.
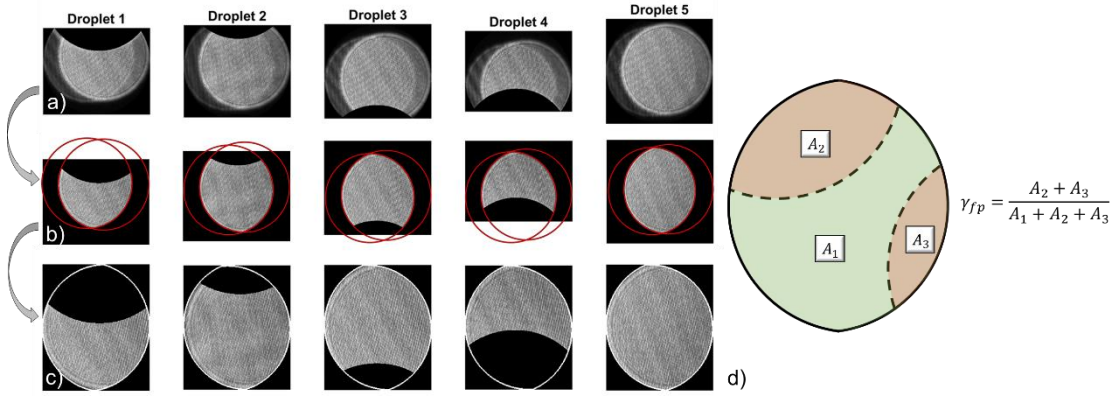

Fig. 18 Extraction and zero padding of the fringe patterns: a) isolated interferograms; b) removal of non-overlapped zones and c) zero padding of the detected fringe pattern region

Fringe frequency information will be extracted by means of a bidimensional FFT. The fifth droplet's fringe pattern shown in Fig. 18c and its corresponding FFT will be used to show the most relevant steps in Fig. 18. Due to the inherent nature of both the considered interferograms and the Fourier transform, in the frequency domain there will be a central high-intensity and low-frequency peak broadening the zero that will be dominant over a series of peaks with varying intensities symmetrically placed two-by-two with respect to the zero-frequency. These pair of peaks represent a measure of the calculated fringe frequencies and its corresponding power spectrum, whereas the low-frequency peak is a measure of background variation (additive disturbances), which is usually lower when compared to fringe variation (multiplicative disturbances) [80].

Depending on interferogram properties such as the signal to noise ratio (SNR), the FFT will usually be rather chaotic and the information extraction quite a cumbersome process, due to the presence of numerous secondary peaks and noise (see Fig 19a). A Gaussian filter is thus implemented in order to smooth the FFT (see Fig 19b) and ease the

25

determination of the fringe frequency. However, since a lot of different frequencies are still present on account of the secondary scattering and image quality, an additional step is then added to filter all undesired frequencies below a certain intensity threshold, which is automatically calculated so as to keep only the three highest intensity peaks.
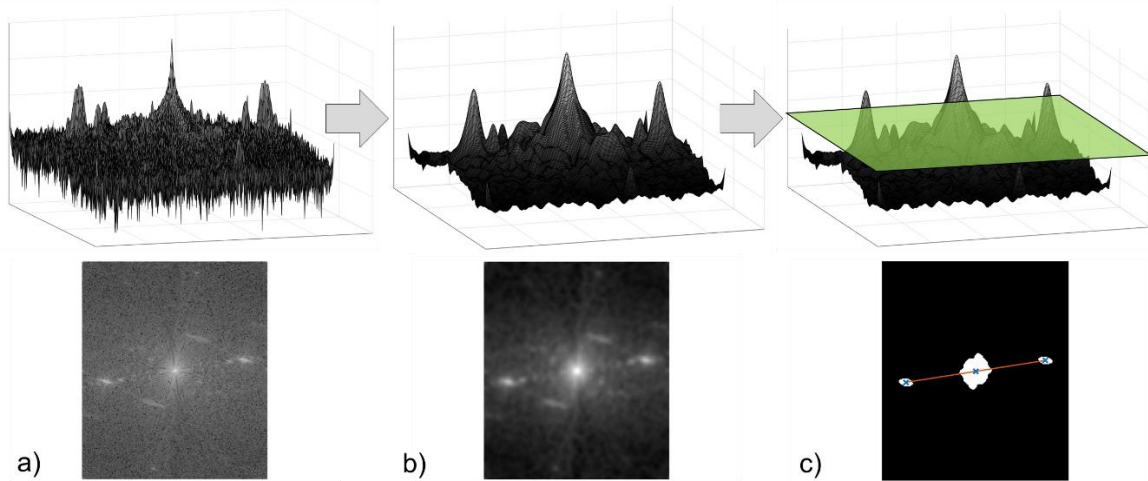

Fig. 19 Tridimensional (upper line) and bidimensional (down line) representation of a) a 2D FFT of a fringe pattern; b) after a Gaussian filter and c) after thresholding the three highest peaks.

By locating and measuring the half-distance between the remaining pair of peaks, the number of fringes contained within the interferogram, and thus the fringe frequency, can be determined. The orientation of the fringe pattern can also be obtained from the direction of the line connecting both peaks. Although said location could be conducted by simply searching for local maxima, the considered peaks are usually quite broad depending on the SNR and image quality, and no clear and distinct peak is present. Therefore, the location is conducted by means of weighted centroids of the power spectrum above the threshold, thus achieving sub-pixel resolution. This approach has been inspired by Natan [81]. Since the Fourier transform determines the relative frequency, i.e. extrapolates the measured fringe frequency to the whole height and width of the considered image, the potential for measuring incomplete fringe patterns should be noted, whether they are vertically or horizontally overlapped. This approach also allows the processing of the typical circular ILIDS interferograms when overlapped.

26

6. Results and discussion

Out-of-focus images were obtained for each one of the three streams of droplets studied. Three representative fragments of the captured images have been extracted and are presented in Fig. 20. In each picture, two circles corresponding to the reflected and refracted light's propagation cone are discernible, with the fringe pattern appearing inside the overlapping region, as discussed in the theoretical background. In Fig. 20a, no overlapping between separate particle interferograms is observed due to the separation between droplets and the reduced droplet size considered, which was around 360 µm. In Fig. 20b, however, vertical overlapping appears. Although the degree of defocus remained the same, droplet size was increased up to about 660 µm. Consequently, the two circles are not as merged as in Fig. 20a on account of the corresponding glare points are farther away from each other. Overlapping also occurs, to a certain degree, when studying droplets of about 850 µm (see Fig. 20c), even though the camera was closer.
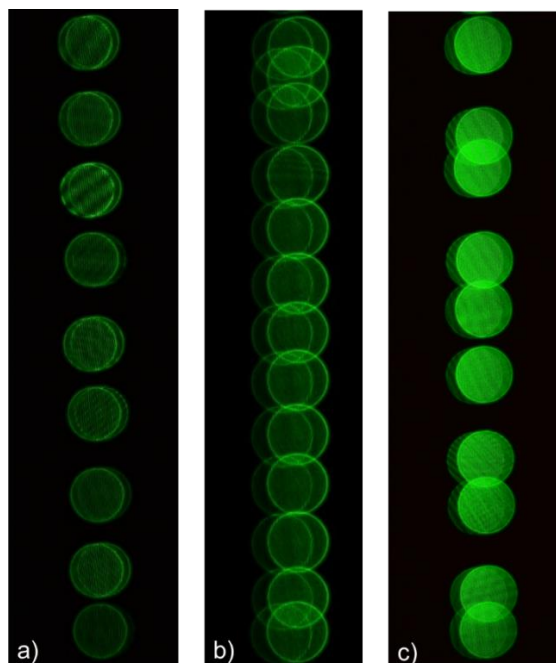
Fig. 20 Experimental results of the tested droplet streams of diameters a) 360µm; b) 660 µm; c) 850 µm.

In order to better assess the image quality of the captured interferograms from each stream of droplets and the differences between them, an isolated fringe pattern has been extracted from each picture and is presented in Fig. 21. The number of pixels covering

each overlapping circle and the resulting fringe pattern is also included as a reference of the particle image size and the degree of overlapping produced between the propagation cones. Since both Fig. 21a and Fig. 21b were captured under the same optical configuration – object distance, field of view, magnification and degree of defocus – the projection of each propagation cone covers the same number of pixels. As stated before, however, the degree of overlapping between them differs, being about a 25% lower in the medium-sized droplet. Finally, the enormous increase in image size of the large droplet (see Fig. 21c) due to the lower object distance and the higher degree of defocus that was needed on account of its incremented diameter should also be noted.
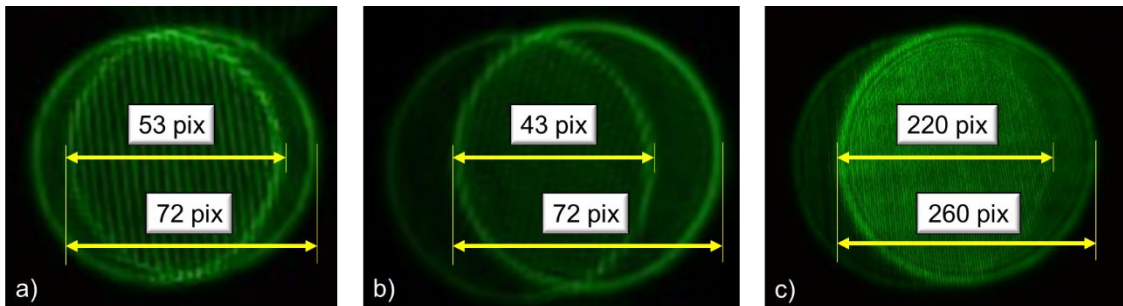
Fig. 21 Isolated interferograms and its corresponding image size and fringe pattern width extracted from the stream of a) small; b) medium-sized and c) large droplets.

Recalling the Nyquist criterion, the number of pixels covered by the fringe pattern must be at least twice the theoretical number of fringes for a given droplet size $n_{pix} \geq 2N$. While both the small and large droplets seem to meet this criterion, the same does not hold true for the medium-sized droplet. The resolution of the CMOS sensor is not enough to adequately sample and capture all the fringes contained within the overlapped propagation cones, and hence the aliasing becomes apparent. For a droplet diameter of 360 µm and a collecting angle of $\alpha = 1.89°$, the theoretical expected number of fringes is approximately $N = 20$. Since the fringe pattern width is $n_{pix} = 53$ pix, the Nyquist criterion is met. Provided the fringe pattern width remained equal to 53 pix, the maximum measurable size would thus be of about 450 - 460 µm. For the larger droplet, the number of fringes expected was $N = 80$, therefore the number of pixel $n_{pix} = 220$ pix met also

the Nyquist criteria. For a droplet diameter of 660 μm, however, the number of expected

fringes increases up to around $N = 37$ for the same collecting angle, whereas the fringe

pattern width not only is not increased but rather reduced down to only $n_{pix} = 43$ pix.

Therefore, due to the inability of the sensor to capture all the fringes and the subsequent

Moiré effect, the fringe pattern shifts. Another pattern with reversed orientation and a

different characteristic frequency emerges, as can be better seen in Fig. 22b below. Fig.

22 also shows the main steps taken during the analysis of each separate interferogram.

In the following subsections the results of the analysis of each case of study will be

presented and discussed accordingly.
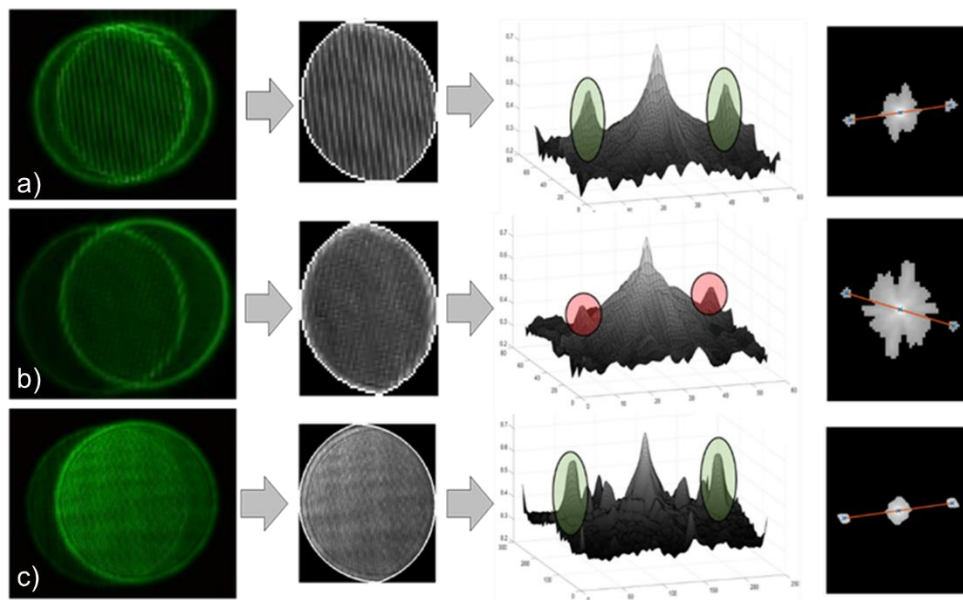
Fig. 22 Image processing procedure of isolated interferograms from the stream of a) small; b) medium-sized and c) large droplets.

6.1 Small Droplets

The first case of study considered is the stream of small droplets, whose mean size was

of about 360 μm. A visual comparison between the three proposed image processing

methods is presented in Fig. 23 for five extracted isolated interferograms. Promising

results are shown concerning the circles detection. Although the Method 2 results (see

Fig. 23c) are somewhat less precise and seem to slightly overestimate the fringe pattern

region, both Methods 1 and 3 (see Fig. 23b and Fig. 23d) show great accuracy. As in

Section 5, Method 2 struggles to find the adequate circles due to the appearance of concentric circular edges around high intensity rings. Low intensity rings also hinder an adequate detection with this method. Particularly good are the results from Method 1, since the detected circles almost perfectly match both high and low intensity rings, even in Droplet 1, in which a quasi-indistinguishable ring is still adequately spotted.
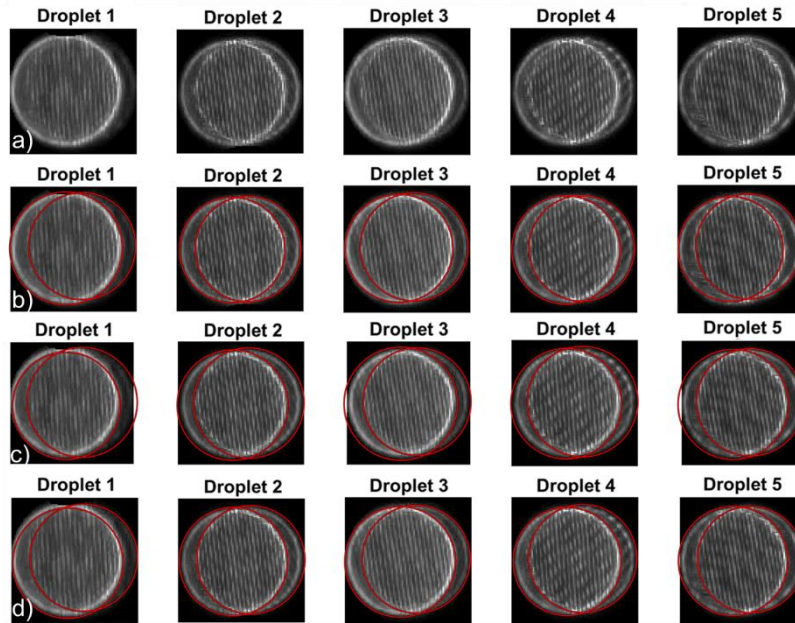
Fig. 23 Visual comparison between the three proposed methods when applied to the stream of small droplets. a) Grayscale ILIDS images; b) method 1; c) method 2 and d) method 3.

A comparison between the experimental results of each method after the implementation of the FFT and the shadowgraph results is presented in Fig. 24a, in which the mean measured diameters along with its uncertainties are shown. The uncertainties are calculated as follows:

$$u = t_{n-1;95.45\%} \frac{\sigma}{\sqrt{n}}$$

As expected after the visual comparison, both Methods 1 and 3 come closer to the shadowgraph results than Method 2. Fig. 24b shows the error of the measured droplet diameter with its relative vertical position for each method. Unlike the shadowgraph

imaging, no dependence on vertical position is observed in the measurement. The error is defined as follows:

$$error(\%) = \frac{|d - d_{ref}|}{d_{ref}} 100.$$
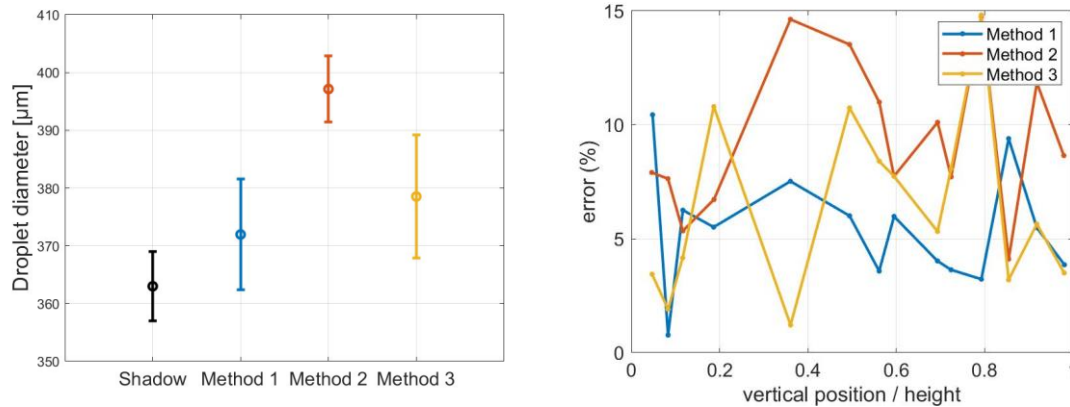
Fig. 24 Comparison between the experimental results of small droplets on the left and the error in the measured diameter vs the relative vertical position of the interferograms on the right.

Although the Method 1 provides the best results in terms of precision as compared to Method 3, there is one singular aspect, however, that favors the Method 3 over the Method 1. The Method 3 algorithm behavior seems to be more robust since only a minor non-essential adjustment in the lower Otsu's threshold was implemented, while the standard deviation in Method 1 of the Gaussian filter had to be tailored and readjusted to the characteristics of these specific interferograms. While a standard deviation of σ = 4 was needed in the large droplets' interferograms, standard deviations higher than σ = 1 considerably worsened the circle detection results when implemented in the small droplets' interferograms. Both the acceptance criteria and the radii range parameters had to be adapted for either method. A higher degree of generality could be achieved for the Method 1 by removing the implementation of both filter prior to the Hough transform, although the accuracy and precision of the approach could consequently be jeopardized, especially whenever the interferogram overlapping is a factor. Nevertheless, method 1 provides less error than the other two methods.
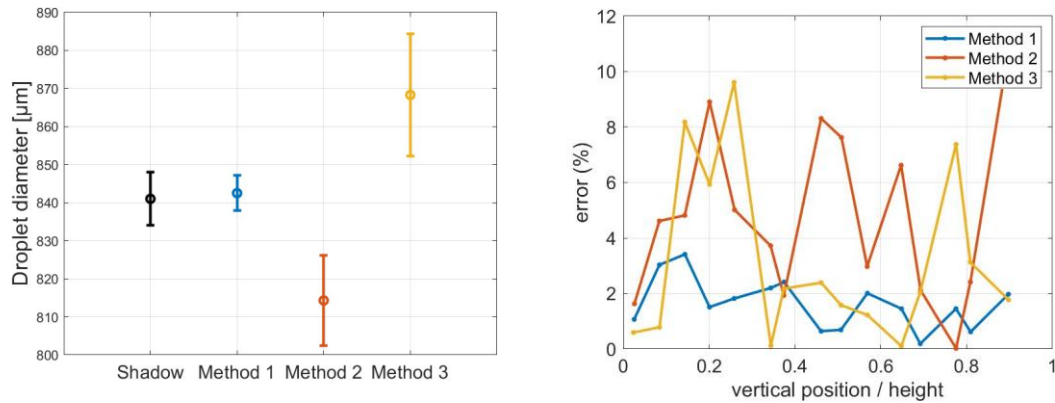
6.3 Large Droplets

A visualization of the circle detection's results provided by each method for the large droplets' interferograms is shown in Fig. 25. Both Methods 1 and 3 provide quite similar results, with no noticeable differences, while some of the Method 2 results underestimate the fringe pattern region. This underestimation, as well as the overestimation in previous subsection, is a consequence of the appearance of concentric borders and the struggle of the algorithm to cope with them. The results of this method will thus have a higher uncertainty and could be somewhat unpredictable.
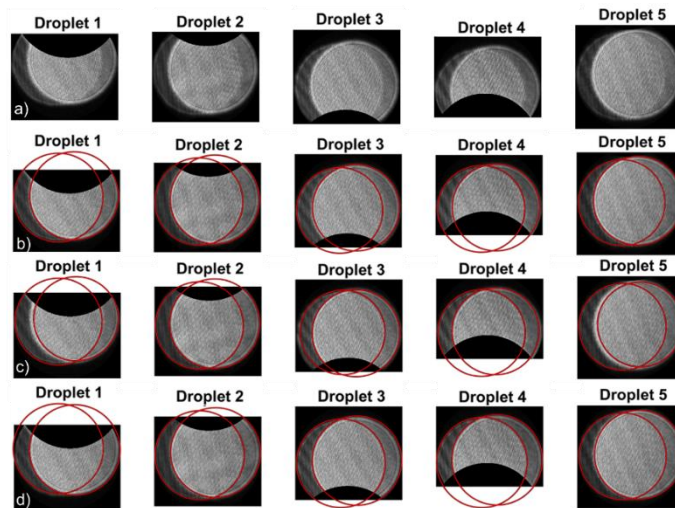
Fig. 25 Visual comparison between the three proposed image processing methods when applied to the stream of large droplets. a) Grayscale ILIDS images; b) method 1; c) method 2 and d) method 3 results.

Fig. 26a shows a comparison of the experimental ILIDS results to those of the shadowgraph imaging technique. Methods 1 seems again to provide excellent results when compared to the shadowgraph imaging, being almost fully contained within its uncertainties. On the other hand, the results provided by Method 2 present a lower accuracy and precision. In the same figure on the right, the error defined as before is presented against the vertical position. It can be observed that Method 3 seems to have less error than Method 2, though the uncertainties are larger.

Fig. 26 Comparison between the experimental results of the stream of large droplets on the left and the error in the measured diameter vs the relative vertical position on the right.

Finally, Fig. 27 shows the evolution of the measured diameters with the degree of overlapping for some measurements. Although there seems to be a slightly increase in the deviation at higher degrees of overlapping, no significant deviations are perceived.
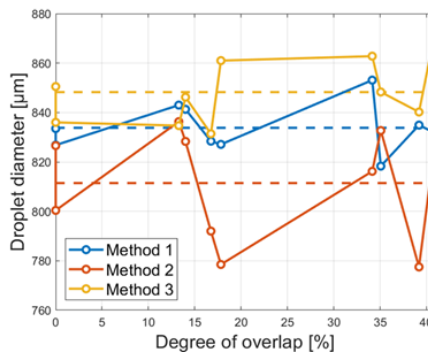

Fig. 27 Evolution of the measured diameter with the degree of overlapping for the stream of large droplets with the three proposed image processing methods.

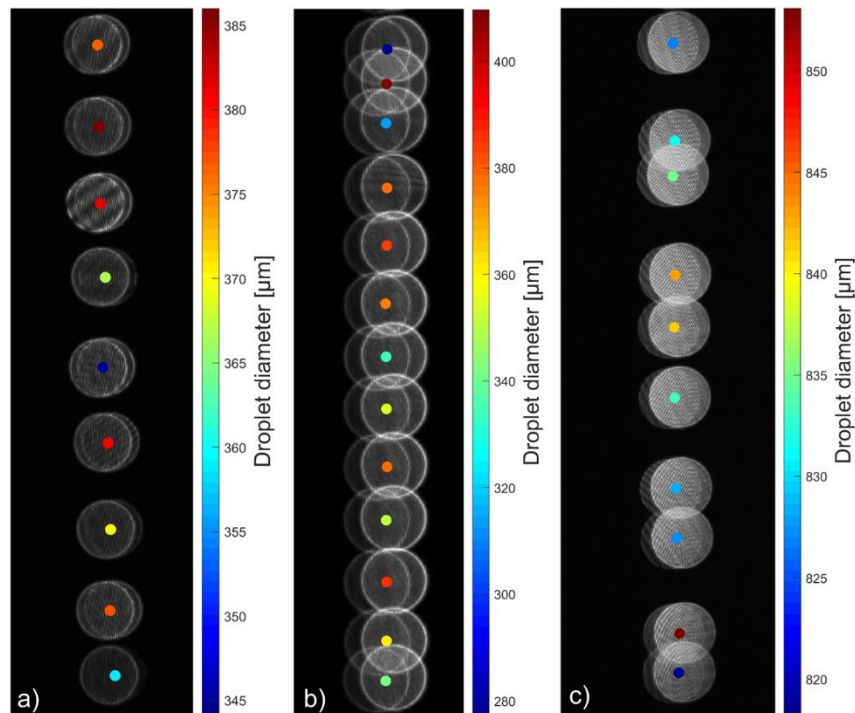*6.4 Reconstruction of the field of droplets*

One of the main advantages of the ILIDS technique is the possibility of providing the bidimensional spatial droplet size distribution. In order to do so, the accurate location of the particle interferograms centroid is needed. However, the presence of mildly to severely overlapped interferograms significantly hinders this task. Nevertheless, the presented approach allows this location even with highly overlapped fringe patterns by means of the two-circle detection and its subsequent fringe pattern zero padding. Although it heavily relies on a successful circle detection, a more adequate particle

33

center can be calculated with great accuracy by taking centroid of the detected fringe pattern region. Fig. 28 shows five isolated fringe patterns extracted from each case of study with its boundaries and centroids underlined.
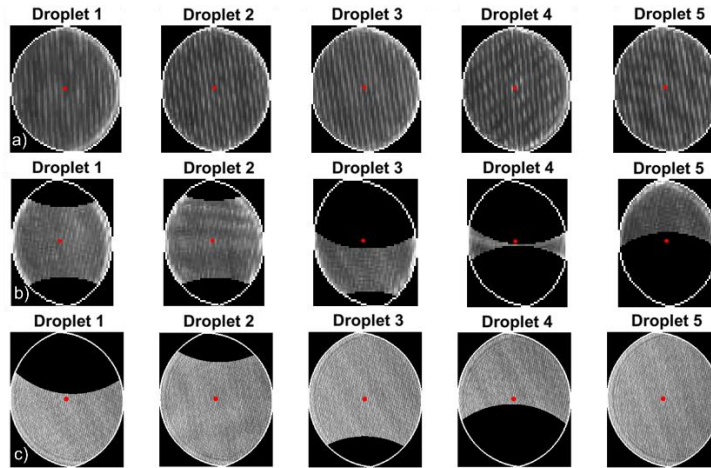
Fig. 28 Isolated interferograms with the detected fringe pattern and its centroid underlined for the stream of a) small; b) medium-sized and c) large droplets.

Having located the local centroid of each fringe pattern, the particle's center can be extrapolated to the original ILIDS image, thus allowing the reconstruction of the spatial droplet field and providing its size distribution. Fig. 29 shows such a reconstruction for each case of study considered. Note that even with severe overlapping and low intensity rings, the algorithm successfully locates with good accuracy the center of the particles. The Method 1 results have been used to illustrate Fig. 29.

Fig. 29 Reconstruction of the spatial droplet field from the stream of a) small; b) medium-sized and c) large droplets.

7. Conclusions

An assessment of the limitations resulting from the implementation of the ILIDS technique inside a wind tunnel with a $3{\times}2\ m^2$ open elliptical test section has been conducted. The main challenge seems to be the minimum object distance needed and the degree of overlapping between droplets' interferograms. As a consequence of the first limitation, a very high resolution is needed so as to comply with the Nyquist criterion and successfully obtain droplet size measurements. On the other hand, on account of the second limitation, a novel approach has been presented based on the droplets not being fully defocused, thus reducing its image size and alleviating the overlap problem. As a result, instead of the usual ILIDS circular interferogram, two whole overlapping circles appear with the fringe pattern emerging withing the overlap region. A novel image processing software has therefore been developed based on the two-circle detection by means of the Hough transform in order to isolate the fringe pattern. To do so, three

different methods have been proposed: two new methods and one based on the literature.

An experimental study at the laboratory on three droplet streams of different sizes has been conducted in order to evaluate the proposed methods and assess the limitations resulting from the long range ILIDS configuration. Two different optical configurations with object distances within the values that would be needed in an actual wind tunnel experiment have been considered. Specifically, an object distance of 1.6 m was used for the large droplets, whereas the medium-sized and small droplets were studied from an object distance of 2.29 m, resulting in field of views of 11.9×7.9 cm^2 and 23.7×15.8 cm^2, respectively. An off-axis angle near 67° under perpendicular polarization of the incident laser sheet has been chosen for the study. All the streams were previously characterized by means of the shadowgraph imaging technique, with the mean diameters and its uncertainties being 363 ± 6 µm, 658 ± 10 µm and 844 ± 7 µm for the small, medium-sized, and large droplets, respectively. Uncertainties were primarily due to the resolution capabilities of the camera, the uneven background illumination, and the inherent uncertainties of the implemented droplet sizing algorithm and the monodispersed stream of droplets.

Both the new proposed methods provide excellent results when compared to the shadowgraph imaging, even with a combination of high and low intensity rings, whereas the method based on the literature struggles to accurately detect said rings. Although only a limited number of droplets have been studied, the resulting uncertainties of the ILIDS results, which can arise on account of the image processing software or the inherent uncertainties within the monodispersed stream of droplets, are presented. For the considered camera resolution of 36.3 megapixels, droplets up to 850 µm and 360 µm were adequately measured at an object distance of 1.6 m and 2.29 m, respectively. Droplets of 650 µm could not be measured at 2.29 m, however, due to the lack of resolution and the non-compliance of the Nyquist criterion. Based on said criterion, it was

calculated that the maximum measurable droplet would have been of about 450 μm, provided the conditions remained the same.

This work provides the basis of future works that should be focused on the limitations that may arise with this approach from horizontal and multiple overlapping, the non-compliance of the Scheimpflug principle regarding the change in image size when studying droplets across the whole field of view and the increase in the maximum measurable droplet size at high object distances.

Acknowledgements

References

[1] F.T. Lynch, A. Khodadoust, Effects of ice accretions on aircraft aerodynamics, Prog. Aerosp. Sci. 37 (2001) 669–767. https://doi.org/10.1016/S0376-0421(01)00018-5.

[2] Federal Aviation Administration, Airplane and Engine Certification Requirements in Supercooled Large Drop, Mixed Phase, and Ice Crystal Icing Conditions, in: Code Fed. Regul., 2014: pp. 65508–65540. https://www.federalregister.gov/d/2014-25789.

[3] Y. Cao, W. Tan, Z. Wu, Aircraft icing: An ongoing threat to aviation safety, Aerosp. Sci. Technol. 75 (2018) 353–385. https://doi.org/10.1016/j.ast.2017.12.028.

[4] W.R. Sand, W.A. Cooper, M.K. Politovich, D.L. Veal, Icing conditions encountered by a research aircraft., J. Clim. Appl. Meteorol. 23 (1984) 1427–1440. https://doi.org/10.1175/0733-3021-23.10.1427

[5] W.A. Cooper, W.R. Sand, M.K. Politovich, D.L. Veal, Effects of icing on performance of a research airplane, J. Aircr. 21 (1984) 708–715. https://doi.org/10.2514/3.45018.

[6] M.K. Politovich, Aircraft icing caused by large supercooled droplets, J. Appl. Meteorol. 28 (1989) 856–868. https://doi.org/10.1175/1520-0450(1989)028<0856:AICBLS>2.0.CO;2.

[7] B.M. Pobanz, J.D. Marwitz, M.K. Politovich, Conditions Associated with Large-Drop Regions, J. Appl. Meteorol. 33 (1994) 1366–1372. https://doi.org/10.1175/1520-0450(1994)033<1366:cawldr>2.0.co;2.

[8] R. Ashenden, J. Marwitz, Characterizing the supercooled large droplet environment with corresponding turboprop aircraft response, J. Aircr. 35 (1998) 912–920. https://doi.org/10.2514/2.2386.

[9] L. Prince Raj, J.W. Lee, R.S. Myong, Ice accretion and aerodynamic effects on a multi-element airfoil under SLD icing conditions, Aerosp. Sci. Technol. 85 (2019) 320–333. https://doi.org/10.1016/j.ast.2018.12.017.

[10] S.G. Cober, G.A. Isaac, J.W. Strapp, Characterizations of aircraft icing environments that include supercooled large drops, J. Appl. Meteorol. 40 (2001) 1984–2002. https://doi.org/10.1175/1520-0450(2001)040<1984:COAIET>2.0.CO;2.

[11] M. Costes, F. Moens, Advanced numerical prediction of iced airfoil aerodynamics, Aerosp. Sci. Technol. 91 (2019) 186–207. https://doi.org/10.1016/j.ast.2019.05.010.

[12] T. Liu, K. Qu, J. Cai, S. Pan, A three-dimensional aircraft ice accretion model based on the numerical solution of the unsteady Stefan problem, Aerosp. Sci. Technol. 93 (2019) 105328. https://doi.org/10.1016/j.ast.2019.105328.

[13] L. Prince Raj, K. Yee, R.S. Myong, Sensitivity of ice accretion and aerodynamic performance degradation to critical physical and modeling parameters affecting airfoil icing, Aerosp. Sci. Technol. 98 (2020) 105659. https://doi.org/10.1016/j.ast.2019.105659.

[14] P. Lopez-Gavilan, A. Velazquez, A. García-Magariño, S. Sor, Breakup criterion for droplets exposed to the unsteady flow generated by an incoming aerodynamic surface, Aerosp. Sci. Technol. 98 (2020) 105687. https://doi.org/10.1016/j.ast.2020.105687.

[15] B.C. Bernstein, F. McDonough, C.A. Wolff, M.K. Politovich, R.M. Rasmussen, S.G. Cober, Diagnosis of supercooled large drop conditions using cloud water content and drop concentration, in: Conf. Aviat. Range, Aerosp. Meteorol., 2004.

[16] S.G. Cober, G.A. Isaac, Characterization of aircraft icing environments with Supercooled Large Drops for application to commercial aircraft certification, J. Appl. Meteorol. Climatol. 51 (2012) 265–284. https://doi.org/10.1175/JAMC-D-11-022.1.

[17] D.N. Anderson, J.-C. Tsao, Ice Shape Scaling for Aircraft in SLD Conditions, Nasa/Cr--2008-215302. (2008). https://ntrs.nasa.gov/archive/nasa/casi.ntrs.nasa.gov/20080043617.pdf

[18] D.M. Orchard, K. Szilder, C.R. Davison, Design of an icing wind tunnel contraction for supercooled large drop conditions, in: 2018 Atmos. Sp. Environ. Conf., 2018. https://doi.org/10.2514/6.2018-3185.

[19] D.M. Orchard, C. Clark, M. Oleskiw, Development of a Supercooled Large Droplet Environment within the NRC Altitude Icing Wind Tunnel, SAE Tech. Pap. 2015-June (2015). https://doi.org/10.4271/2015-01-2092.

[20] J.-P. Douzals, M. Alheidary, C. Sinfort, In situ droplet size measurements in a wind tunnel, Asp. Appl. Biol. 137 (2018) 237-244.

[21] C. Ruan, F. Chen, W. Cai, Y. Qian, L. Yu, X. Lu, Principles of non-intrusive diagnostic techniques and their applications for fundamental studies of combustion instabilities in gas turbine combustors: A brief review, Aerosp. Sci. Technol. 84 (2019) 585–603. https://doi.org/10.1016/j.ast.2018.10.002.

[22] A. de Araújo Coelho, J.L. Brenguier, T. Perrin, Droplet spectra measurements with the FSSP-100. Part II: Coincidence effects, J. Atmos. Ocean. Technol. 22 (2005) 1756–1761. https://doi.org/10.1175/JTECH1818.1.

[23] J.L. Brenguier, T. Bourrianne, A.A. De Coelho, J. Isbert, R. Peytavi, D. Trevarin, P. Weschler, Improvements of droplet size distribution measurements with the fast-FSSP (Forward Scattering Spectrometer Probe), J. Atmos. Ocean. Technol. 15 (1998) 1077–1090. https://doi.org/10.1175/1520-0426(1998)015<1077:IODSDM>2.0.CO;2.

[24] W.D. Bachalo, M.J. Houser, Phase/Doppler Spray Analyzer for Simultaneous Measurements of Drop Size and Velocity Distributions, Opt. Eng. 23 (1984) 583–590. https://doi.org/10.1117/12.7973341.

[25] C. Li, C. Li, F. Xiao, Q. Li, Y. Zhu, Experimental study of spray characteristics of liquid jets in supersonic crossflow, Aerosp. Sci. Technol. 95 (2019) 105426. https://doi.org/10.1016/j.ast.2019.105426.

[26] G. König, K. Anders, A. Frohn, A new light-scattering technique to measure the diameter of periodically generated moving droplets, J. Aerosol Sci. 17 (1986) 157–167. https://doi.org/10.1016/0021-8502(86)90063-7.

[27] R. Ragucci, A. Cavaliere, P. Massoli, Drop Sizing by Laser Light Scattring Exploiting Intensity Angular Oscillation in the mie regime, Part. Part. Syst. Charact. 7 (1990) 221–225. https://doi.org/10.1002/ppsc.19900070136.

[28] K.H. Hesselbacher, K. Anders, A. Frohn, Experimental investigation of Gaussian beam effects on the accuracy of a droplet sizing method, Appl. Opt. 30 (1991) 4930. https://doi.org/10.1364/ao.30.004930.

[29] N. Roth, K. Anders, A. Frohn, Refractive-index measurements for the correction of particle sizing methods, Appl. Opt. 30 (1991) 4960. https://doi.org/10.1364/ao.30.004960.

[30] A.R. Glover, S.M. Skippon, R.D. Boyle, Interferometric laser imaging for droplet sizing: a method for droplet-size measurement in sparse spray systems, Appl. Opt. 34 (1995) 8409. https://doi.org/10.1364/ao.34.008409.

[31] H.C. van de Hulst, R.T. Wang, Glare points, Appl. Opt. 30 (1991) 4755. https://doi.org/10.1364/ao.30.004755.

[32] S. Dehaeck, J.P.A.J. Van Beeck, M.L. Riethmuller, Extended glare point velocimetry and sizing for bubbly flows, Exp. Fluids. 39 (2005) 407–419. https://doi.org/10.1007/s00348-005-1004-6.

[33] T. Girasole, K.F. Ren, D. Lebrun, G. Gouesbet, G. Gréhan, Particle Imaging Sizing: GLMT Simulations, J. Vis. 3 (2000) 195–202. https://doi.org/10.1007/BF03182412.

[34] W.J. Glantschnig, S.-H. Chen, Light scattering from water droplets in the geometrical optics approximation, Appl. Opt. 20 (1981) 2499. https://doi.org/10.1364/ao.20.002499.

[35] A. Ungut, G. Grehan, G. Gouesbet, Comparisons between geometrical optics and Lorenz-Mie theory, Appl. Opt. 20 (1981) 2911. https://doi.org/10.1364/ao.20.002911.

[36] N. Damaschke, H. Nobach, C. Tropea, Optical limits of particle concentration for multi-dimensional particle sizing techniques in fluid mechanics, Exp. Fluids. 32 (2002) 143–152. https://doi.org/10.1007/s00348-001-0371-x.

[37] K. Zarogoulidis, Y. Hardalupas, A.M.K.P. Taylor, Theoretical evaluation of droplet concentration limits for interferometric droplet sizing measurements, in: 16th Int. Symp. Appl. Laser Tech. Fluid Mech., Lisbon, 2012.

[38] H. Bocanegra Evans, N. Dam, D. Van Der Voort, G. Bertens, W. Van De Water, Measuring droplet size distributions from overlapping interferometric particle images, Rev. Sci. Instrum. 86 (2015). https://doi.org/10.1063/1.4909537.

[39] M. Maeda, T. Kawaguchi, K. Hishida, Novel interferometric measurement of size and velocity distributions of spherical particles in fluid flows, Meas. Sci. Technol. 11 (2000). https://doi.org/10.1088/0957-0233/11/12/101.

[40] T. Kawaguchi, T. Kobayashi, M. Maeda, Measurement of spray flow by an improved Interferometric Laser Imaging Droplet Sizing (ILIDS) system, in: Laser Tech. Fluid Mech., Springer, Berlin, Heidelberg, 2002: pp. 209–220. https://doi.org/10.1007/978-3-662-08263-8_13.

[41] N. Damaschke, H. Nobach, T.I. Nonn, N. Semidetnov, C. Tropea, Size and velocity measurements with the global phase Doppler technique, in: 11th Int. Symp. Appl. Laser Tech. to Fluid Mech., Lisbon, 2002: pp. 1–11.

[42] E. Porcheron, P. Lemaitre, J. Van Beeck, R. Vetrano, M. Brunel, G. Grehan, L. Guiraud, Development of a spectrometer for airborne measurement of droplet sizes in clouds, J. Eur. Opt. Soc. 10 (2015) 1–6. https://doi.org/10.2971/jeos.2015.15030.

[43] C. Dunker, C. Roloff, A. Grassmann, Interferometric laser imaging for in-flight cloud droplet sizing, Meas. Sci. Technol. 27 (2016). https://doi.org/10.1088/0957-0233/27/12/124004.

[44] J. Jacquot Kielar, Y. Wu, S. Coëtmellec, D. Lebrun, G. Gréhan, M. Brunel, Size determination of mixed liquid and frozen water droplets using interferometric out-of-focus imaging, J. Quant. Spectrosc. Radiat. Transf. 178 (2016) 108–116. https://doi.org/10.1016/j.jqsrt.2015.09.009.

[45] M. Brunel, S. González Ruiz, J. Jacquot, J. van Beeck, On the morphology of irregular rough particles from the analysis of speckle-like interferometric out-of-focus images, Opt. Commun. 338 (2015) 193–198. https://doi.org/10.1016/j.optcom.2014.10.053.

[46] M. Brunel, S. Coetmellec, G. Gréhan, H. Shen, Interferometric out-of-focus imaging simulator for irregular rough particles, J. Eur. Opt. Soc. 9 (2014). https://doi.org/10.2971/jeos.2014.14008.

[47] A. Querel, P. Lemaitre, M. Brunel, E. Porcheron, G. Gréhan, Real-time global interferometric laser imaging for the droplet sizing (ILIDS) algorithm for airborne research, Meas. Sci. Technol. 21 (2010). https://doi.org/10.1088/0957-0233/21/1/015306.

[48] H. Shen, M. Brunel, G. Grehan, A. Querel, P. Lemaitre, E. Porcheron, Algorithm improvement for real time ILIDS analysis in airborne research, in: Prog. Electromagn. Res. Symp., 2011: pp. 160-163.

[49] M. Brunel, H. Shen, Design of ILIDS configurations for droplet characterization, Particuology. 11 (2013) 148–157. https://doi.org/10.1016/j.partic.2012.06.014.

[50] H. Shen, S. Coëtmellec, G. Gréhan, M. Brunel, Interferometric laser imaging for droplet sizing revisited: Elaboration of transfer matrix models for the description of complete systems, Appl. Opt. 51 (2012) 5357–5368. https://doi.org/10.1364/AO.51.005357.

[51] L. Qieni, J. Wenhua, L. Tong, W. Xiang, Z. Yimo, High-accuracy particle sizing by interferometric particle imaging, Opt. Commun. 312 (2014) 312–318. https://doi.org/10.1016/j.optcom.2013.09.049.

[52] L. Qieni, H. Kan, G. Baozhen, W. Xiang, High-accuracy simultaneous measurement of particle size and location using interferometric out-of-focus imaging, Opt. Express. 24 (2016) 16530. https://doi.org/10.1364/oe.24.016530.

[53] H. Yuen, J. Princen, J. Illingworth, J. Kittler, Comparative study of Hough Transform methods for circle finding, Image Vis. Comput. 8 (1990) 71–77. https://doi.org/10.1016/0262-8856(90)90059-E

[54] Z. Xu, A high accurate static contact angle algorithm based on Hough transformation, Measurement 55 (2014) 97–100. https://doi.org/10.1016/j.measurement.2014.04.030.

[55] F. Meyer, Topographic distance and watershed lines, Signal Processing. 38 (1994) 113–125. https://doi.org/10.1016/0165-1684(94)90060-4

[56] H. Zhang, Z. Tang, Y. Xie, X. Gao, Q. Chen, A watershed segmentation algorithm based on an optimal marker for bubble size measurement, Measurement 138 (2019) 182–193. https://doi.org/10.1016/j.measurement.2019.02.005.

[57] A. Jahedsaravani, M. Massinaei, M.H. Marhaban, An image segmentation algorithm for measurement of flotation froth bubble size distributions, Measurement 111 (2017) 29–37. https://doi.org/10.1016/j.measurement.2017.07.023.

[58] L.S. Zhai, X.Y. Li, P. Bian, N. De Jin, Measurement of droplet sizes in bubbly oil-in-water flows using a fluid-sampling device, Measurement 102 (2017) 296–308. https://doi.org/10.1016/j.measurement.2017.01.055.

[59] X. Yang, T. Ren, L. Tan, Size distribution measurement of coal fragments using digital imaging processing, Measurement 160 (2020) 107867. https://doi.org/10.1016/j.measurement.2020.107867.

[60] Y. Hardalupas, S. Sahu, A.M.K.P. Taylor, K. Zarogoulidis, Simultaneous planar measurement of droplet velocity and size with gas phase velocities in a spray by

combined ILIDS and PIV techniques, Exp. Fluids. 49 (2010) 417–434. https://doi.org/10.1007/s00348-009-0802-7.

[61] J. Madsen, J. Harbo, T.I. Nonn, D. Blondel, B.H. Hjertager, T. Solberg, Measurement of droplet size and velocity distributions in sprays using Interferometric Particle Imaging (IPI) and Particle Tracking Velocimetry (PTV), in: Proc. INCLASS Conf., 2003: pp. 13–17.

[62] Y. Akasaka, T. Kawaguchi, M. Maeda, Application of Interferometric Laser Imaging Technique to a Transient Spray Flow, in: 11th Int. Symp. Appl. Laser Tech. to Fluid Mech., 2002.

[63] S. Kosch, N. Ashgriz, Eliminating center discrepancies between simultaneously captured ILIDS and PIV images by means of direct homography estimation, Measurement 94 (2016) 12–18. https://doi.org/10.1016/j.measurement.2016.07.063.

[64] L. V. Lorenz, Lysbevægelser i og uden for en af plane Lysbølger belyst Kugle, Det K. Danske Vidensk. Selsk. Skr. 6 (1890) 1–62.

[65] G. Mie, Beiträge zur Optik trüber Medien, speziell kolloidaler Metallösungen, Ann. Phys. 330 (1908) 377–445. https://doi.org/10.1002/andp.19083300302

[66] P. Debye, Das elektromagnetische feld um einen zylinder und die theorie des Regenbogens, Phys. Zeitschrift. 9 (1908) 775–778.

[67] H.M. Nussenzveig, High-frequency scattering by a transparent sphere. I. Direct reflection and transmission, J. Math. Phys. 10 (1969) 82–124. https://doi.org/10.1063/1.1664764

[68] P. Laven, MiePlot, (2018). http://www.philiplaven.com/mieplot.htm (accessed March 20, 2020).

[69] J. Xu, B. Ge, Q. Lu, Wide-range and accurate particle sizing using extended interferometric particle imaging technique, Rev. Sci. Instrum. 89 (2018). https://doi.org/10.1063/1.5058711.

[70] J. Jacquot, M. Talbi, M. Brunel, Third glare point effect in 90°Interferometric Laser Imaging for Droplet Sizing, Opt. Commun. 462 (2020) 125349. https://doi.org/10.1016/j.optcom.2020.125349.

[71] Light scattering by small particles. By H. C. van de Hulst. New York (John Wiley and Sons), London (Chapman and Hall), 1957. Pp. xiii, 470; 103 Figs.; 46 Tables. 96s, Q. J. R. Meteorol. Soc. 84 (1958) 198–199. https://doi.org/10.1002/qj.49708436025.

[72] C. Mounaïm-Rousselle, O. Pajot, Droplet sizing by Mie scattering interferometry in a spark ignition engine, Part. Part. Syst. Charact. 16 (1999) 160–168. https://doi.org/10.1002/(SICI)1521-4117(199908)16:4<160::AID-PPSC160>3.0.CO;2-G.

[73] Lord Rayleigh, On the instability of jets, Proc. London Math. Soc. s1-10 (1878) 4–13. https://doi.org/10.1112/plms/s1-10.1.4

[74] D. Bradley, G. Roth, Adaptive Thresholding using the Integral Image, J. Graph. Tools. 12 (2007) 13–21. https://doi.org/10.1080/2151237x.2007.10129236

[75] N. Otsu, Threshold Selection Method From Gray-Level Histograms., IEEE Trans Syst Man Cybern. SMC-9 (1979) 62–66. https://doi.org/10.1109/tsmc.1979.4310076

[76] J.B.T.M. Roerdink, Group morphology, Pattern Recognit. 33 (2000) 877–895. https://doi.org/10.1016/S0031-3203(99)00152-1

[77] P. Soille, Morphological Image Analysis: Principles and Applications, 2004, pp. 170-171. https://doi.org/10.1007/978-3-662-06431-3.

[78] J. Canny, A Computational Approach to Edge Detection, IEEE Trans. Pattern Anal. Mach. Intell. PAMI-8 (1986) 679–698. https://doi.org/10.1109/TPAMI.1986.4767851

[79] S.J. Orfanidis, Noise Reduction and Signal Enhancement, Rutgers University, 2010. https://www.ece.rutgers.edu/~orfanidi/intro2sp/orfanidis-i2sp.pdf

[80] G.T. Nehmetallah, R. Aylo, L.A. Williams, G.T. Nehmetallah, R. Aylo, L.A. Williams, Fringe Deciphering Techniques Applied to Analog Holographic Interferometry, in: Analog Digit. Hologr. with MATLAB, 2015: pp. 84–90. https://doi.org/10.1117/3.2190844.ch3

[81] A. Natan, Fast 2D peak finder, MATLAB Cent. File Exch. (2012). http://www.mathworks.com/matlabcentral/fileexchange/37388-fast-2d-peak-finder (accessed August 23, 2019).

[82] M. Brunel, M. Talbi, S. Coetmellec, G. Grehan, Y. Wu, and J. Jacquot-Kielar, "Interferometric out-of-focus imaging of freezing droplets," Opt. Commun. 433, 173-182 (2019).

[83] A. Palatano, C. M. García and A. Rodríguez "Rectification of Image Velocity Results (RIVeR): A simple and user-friendly toolbox for large scale water surface Particle Image Velocimetry (PIV) and Particle Tracking Velocimetry (PTV)" Computers and Geosciences 109, 323-330 (2017).

[84] S. Santosh Kumar, Cheng Li, Chase E. Christen, Christopher J. Hogan, Steven A. Fredericks, Jiarong Hong, Automated droplet size distribution measurements using digital inline holography, J. of Aerosol Sci., 137 (2019) 105442,https://doi.org/10.1016/j.jaerosci.2019.105442.

[85] Poursadegh, F., Bibik, O., Yraguen, B., & Genzale, C. L. (2020). A multispectral, extinction-based diagnostic for drop sizing in optically dense diesel sprays. International Journal of Engine Research, 21(1), 15–25. https://doi.org/10.1177/1468087419866034.

[86] F. Onofri and S. Barbosa, "Chapter II: Optical particle characterization," in Laser Metrology in Fluid Mechanics, A. Boutier, ed. (Wiley-ISTE, London, 2012).